iLQR-VAE : CONTROL-BASED LEARNING OF INPUT-DRIVEN DYNAMICS WITH APPLICATIONS TO NEURAL DATA

Anonymous authors
Paper under double-blind review

ABSTRACT

Understanding how neural dynamics give rise to behaviour is one of the most fundamental questions in systems neuroscience. To achieve this, a common approach is to record neural populations in behaving animals, and model these data as emanating from a latent dynamical system whose state trajectories can then be related back to behavioural observations via some form of decoding. As recordings are typically performed in localized circuits that form only a part of the wider implicated network, it is important to simultaneously learn the local dynamics and infer any unobserved external input that might drive them. Here, we introduce iLQR-VAE, a novel control-based approach to variational inference in nonlinear dynamical systems, capable of learning both latent dynamics, initial conditions, and ongoing external inputs. As in recent deep learning approaches, our method is based on an input-driven sequential variational autoencoder (VAE). The main novelty lies in the use of the powerful iterative linear quadratic regulator algorithm (iLQR) in the recognition model. Optimization of the standard evidence lower-bound requires differentiating through iLQR solutions, which is made possible by recent advances in differentiable control. Importantly, having the recognition model implicitly defined by the generative model greatly reduces the number of free parameters and allows for flexible, high-quality inference. This makes it possible for instance to evaluate the model on a single long trial after training on smaller chunks. We demonstrate the effectiveness of iLQR-VAE on a range of synthetic systems, with autonomous as well as input-driven dynamics. We further apply it to neural and behavioural recordings in non-human primates performing two different reaching tasks, and show that iLQR-VAE yields high-quality kinematic reconstructions from the neural data.

1 INTRODUCTION

The mammalian brain is a complex, high-dimensional system, containing billions of neurons whose coordinated dynamics ultimately drives behaviour. Identifying and interpreting these dynamics is the focus of a large body of neuroscience research, which is being facilitated by the advent of new experimental techniques that allow large-scale recordings of neural populations (Jun et al., 2017; Stosiek et al., 2003). A range of methods have been developed for learning dynamics from data (Buesing et al., 2012; Gao et al., 2016; Duncker et al., 2019; Archer et al., 2015; Hernandez et al., 2018; She and Wu, 2020; Kim et al., 2021; Nguyen et al., 2020). These methods all specify a generative model in the form of a flexible latent dynamical system driven by process noise, coupled with an appropriate observation model.

However, neural recordings are typically only made in a small selection of brain regions, leaving many areas unobserved which might provide relevant task-related input to the recorded one(s). Yet, the aforementioned methods perform Bayesian inference of state trajectories directly, and therefore do not support inference of external input (which they effectively treat as process noise and marginalize out). Indeed, simultaneous learning of latent dynamics *and* inference of unobserved control inputs is a challenging problem that involves teasing apart momentary variations in the data that can be attributed to the system's internal transition function, and those that need to be explained

by unobserved inputs. This distinction can be achieved by introducing external control in the form of abrupt changes in the latent state transition function, and inferring these switching events (Ghahramani and Hinton, 2000; Linderman et al., 2017). More recently, Pandarinath et al. (2018) introduced LFADS, a sequential variational autoencoder (VAE) that performs inference at the level of external inputs as well as initial latent states. The inferred inputs were shown to be congruent with task-induced perturbations in various reaching tasks in primates (Pandarinath et al., 2018; Keshtkaran et al., 2021).

Here, we introduce iLQR-VAE, a new method for learning input-driven latent dynamics from data. As in LFADS, we use an input-driven sequential VAE to encode observations into a set of initial conditions and external inputs driving an RNN generator. However, while LFDADS uses a separate, bidirectional RNN as the encoder, here we substitute the inference network with an *optimization-based recognition model* that relies on the powerful iterative linear quadratic regulator algorithm (iLQR, Li and Todorov, 2004). iLQR solves an optimization problem that finds a mode of the exact posterior over inputs for the current setting of generative parameters. This ensures that the encoder mean remains optimal for every update of the decoder, thus reducing the amortization gap (Cremer et al., 2018). Moreover, having the recognition model implicitly defined by the generative model stabilizes training, circumvents the need for tricks such as KL warmup, and greatly reduces the number of (hyper-)parameters.

While iLQR-VAE could find applications in many fields as a general approach to learning stochastic nonlinear dynamical systems, here we focus on neuroscience case studies. We first demonstrate in a series of synthetic examples that iLQR-VAE can recover the true dynamics in both autonomous and input-driven systems. Next, we show state-of-the art performance on monkey M1 population recordings during two types of reaching tasks (O'Doherty et al., 2018; Churchland et al., 2010). In particular, we show that hand kinematics can be accurately decoded from inferred latent state trajectories, and that the inferred inputs are consistent with recently proposed theories of motor preparation.

2 Method

iLQR-VAE models a set of temporal observations, such as behavioural and/or neural recordings, through a shared input-driven nonlinear latent dynamical system. The input encapsulates both process noise (as in traditional latent dynamics models), initial inputs that set the initial condition of the dynamics, and any meaningful task-related control input. In this section, we describe the architecture of the generative model, and the control-based variational inference strategy used for training the model and making predictions (graphical summary in Appendix A).

2.1 Generative model

We consider the following generative model:

$$\text{latent state} \quad \boldsymbol{z}_{t+1} = f_\theta(\boldsymbol{z}_t, \boldsymbol{u}_t, t) \tag{1}$$

$$\text{observations} \quad \boldsymbol{o}_t|\boldsymbol{z}_t \sim p_\theta(\boldsymbol{o}_t|\boldsymbol{z}_t) \tag{2}$$

where $\boldsymbol{u}_t \in \mathbb{R}^m$, $\boldsymbol{z}_t \in \mathbb{R}^n$ and $\boldsymbol{o}_t \in \mathbb{R}^{n_o}$ are the input, latent state and observations at time t, respectively. Here, observations may comprise either neural activity, behavioural variables, or both – the distinction will be made later where relevant. We use the notation θ to denote the set of all parameters of the generative model. We use $\boldsymbol{u}_0$ to set the initial condition $\boldsymbol{z}_1 = f_\theta(\boldsymbol{0}, \boldsymbol{u}_0, 0)$ of the network[1]. This way, the latent state trajectory of the network $\boldsymbol{z}(\boldsymbol{u}) = \{\boldsymbol{z}_1, \ldots, \boldsymbol{z}_T\}$ is entirely determined by the input sequence $\boldsymbol{u} = \{\boldsymbol{u}_0, \ldots, \boldsymbol{u}_T\}$ and the state transition function $f_\theta(\cdot)$, according to Equation 1. For $f_\theta(\cdot)$, we use either standard linear or GRU-like RNN dynamics (see Appendix B for details). For the likelihoods, we use Gaussian or Poisson distributions with means given by linear or nonlinear readouts of the network state of the form $\bar{\boldsymbol{o}}_t = h(\boldsymbol{C}\boldsymbol{z}_t + \boldsymbol{b})$ (Appendix C).

[1]Note that when $m < n$, $\boldsymbol{u}_0$ can only reach an m-dimensional subspace of initial conditions, which could be limiting. We can circumvent this problem by spreading $\boldsymbol{u}_0$ over multiple surrogate time bins before the start of the trial, i.e. introduce $\{\boldsymbol{u}_{-n/m}, \ldots, \boldsymbol{u}_{-2}, \boldsymbol{u}_{-1}, \boldsymbol{u}_0\}$ together with an appropriate dependence of f_θ on $t \leq 0$ in Equation 1, such that each of these surrogate inputs target a different latent subspace with purely integrating ("sticking") linear dynamics before $t = 1$.

We place a Gaussian prior over $\boldsymbol{u}_{t<=0}$. We then consider two alternative choices for the prior over $\boldsymbol{u}_{t>0}$. The first is a Gaussian prior

$$p_\theta(\boldsymbol{u}_{t>0}) = \mathcal{N}(0, \boldsymbol{S}^2) \tag{3}$$

with $\boldsymbol{S} = \text{diag}(s_1, \ldots, s_m)$. In many settings however, we expect inputs to enter the system in a sparse manner. To explicitely model this, we introduce a second prior over $\boldsymbol{u}$ in the form of a heavy-tailed distribution constructed hierarchically by assuming that the ith input at time $t > 0$ is

$$u_{it} = s_i \epsilon_{it} \sqrt{\nu / \alpha_t} \tag{4}$$

where $s_i > 0$ is a scale factor, $\epsilon_{it} \sim \mathcal{N}(0, 1)$ is independent across i and t, and $\alpha_t \sim \chi^2_\nu$ is a shared scale factor drawn from a chi-squared distribution with ν degrees of freedom. Thus, inputs are spatially and temporally independent a priori, such that any spatio-temporal structure in the observations will have to be explained by the coupled dynamics of the latent states. Moreover, the heavy-tailed nature of this prior allows for strong inputs when they are needed. Finally, the fact that the scale factor is shared across input dimensions means that inputs are either all weak or potentially all strong at the same time for all input channels, expressing the prior belief that inputs come as shared events.

This hierarchical construction induces a multivariate Student prior:

$$p_\theta(\boldsymbol{u}_t) = \frac{\Gamma\left[(\nu + m)/2\right]}{\Gamma\left[\nu/2\right](\nu\pi)^{m/2}|\boldsymbol{S}|} \left[1 + \frac{1}{\nu}\boldsymbol{u}_t^T \boldsymbol{S}^{-2} \boldsymbol{u}_t\right]^{-(\nu+m)/2} \tag{5}$$

where $\boldsymbol{S} = \text{diag}(s_1, \ldots, s_m)$. Note that both $\boldsymbol{S}$ and ν are parameters of the generative model, which we will learn.

2.2 iLQR-VAE: A NOVEL VARIATIONAL INFERENCE STRATEGY

To train the model, we optimize θ to maximize the log-likelihood of observing a collection of independent observation sequences $\boldsymbol{\mathcal{O}} = \{\boldsymbol{o}^{(1)}, \ldots, \boldsymbol{o}^{(K)}\}$, or "trials", given by:

$$\log p_\theta(\boldsymbol{\mathcal{O}}) = \sum_{k=1}^{K} \log \int p_\theta(\boldsymbol{o}^{(k)} | \boldsymbol{z}(\boldsymbol{u})) p_\theta(\boldsymbol{u})\, d\boldsymbol{u}. \tag{6}$$

As the integral is in general intractable, we resort to an amortized variational inference strategy by introducing a recognition model $q_\phi(\boldsymbol{u}|\boldsymbol{o}^{(k)})$ to approximate the posterior $p_\theta(\boldsymbol{u}|\boldsymbol{o}^{(k)})$. Following standard practice (Kingma and Welling, 2013; Rezende et al., 2014), we thus train the model by maximizing the evidence lower-bound (ELBO):

$$\begin{aligned}
\mathcal{L}(\boldsymbol{\mathcal{O}}, \theta, \phi) &= \sum_k \mathbb{E}_{q_\phi(\boldsymbol{u}|\boldsymbol{o}^{(k)})} \left[\log p_\theta(\boldsymbol{o}^{(k)}|\boldsymbol{u}) + \log p_\theta(\boldsymbol{u}) - \log q_\phi(\boldsymbol{u}|\boldsymbol{o}^{(k)})\right] && (7)\\
&= \sum_k \mathbb{E}_{q_\phi(\boldsymbol{u}|\boldsymbol{o}^{(k)})} \left[\sum_{t=1}^{T} \log p_\theta(\boldsymbol{o}_t^{(k)}|\boldsymbol{z}_t) + \log p_\theta(\boldsymbol{u}_t) - \log q_\phi(\boldsymbol{u}_t|\boldsymbol{o}^{(k)})\right] && (8)\\
&\leq \log p_\theta(\boldsymbol{\mathcal{O}}). && (9)
\end{aligned}$$

with respect to both θ and ϕ.

Here, the main novelty is the use of an optimization-based recognition model. We reason that maximizing the exact log posterior, i.e. computing

$$\begin{aligned}
\boldsymbol{u}^\star(\boldsymbol{o}^{(k)}) &= \underset{\boldsymbol{u}}{\text{argmax}} \log p_\theta(\boldsymbol{u}|\boldsymbol{o}^{(k)}) && (10)\\
&= \underset{\boldsymbol{u}}{\text{argmax}} \left[\sum_{t=1}^{T} \log p_\theta(\boldsymbol{o}_t^{(k)}|\boldsymbol{u}) + \log p_\theta(\boldsymbol{u}_t)\right] && (11)
\end{aligned}$$

subject to the generative dynamics of Equations 1 and 2, is a standard nonlinear control problem: $\log p_\theta(\boldsymbol{o}_t^{(k)}|\boldsymbol{u})$ acts as a running cost penalizing momentary deviations between desired outputs $\boldsymbol{o}_t$ and actual outputs given a set of controls $\boldsymbol{u}$, and $\log p_\theta(\boldsymbol{u}_t)$ acts as an energetic cost on those

controls. Importantly, there exists a general purpose, efficient algorithm to solve such nonlinear control problems: iLQR (Li and Todorov, 2004; Appendix D). We thus propose to use a black-box iLQR solver to parameterize the mean of the recognition density $q_\phi(\boldsymbol{u}|\boldsymbol{o})$ for any $\boldsymbol{o}$, and to model uncertainty separately using a multivariate Gaussian density common to all trials. Therefore, we parametrize the recognition model as follows:

$$q_\phi(\boldsymbol{u}|\boldsymbol{o}) = \mathcal{N}(\boldsymbol{u}; \boldsymbol{u}^\star(\boldsymbol{o}), \boldsymbol{\Sigma}_{\text{s}} \otimes \boldsymbol{\Sigma}_{\text{t}}) \tag{12}$$

$$\text{with } \boldsymbol{u}^\star(\boldsymbol{o}) = \text{iLQRsolve}(\boldsymbol{o}, \theta). \tag{13}$$

where we use a separable posterior covariance (the Kronecker product of a spatial factor $\boldsymbol{\Sigma}_{\text{s}}$ and a temporal factor $\boldsymbol{\Sigma}_{\text{t}}$).

To optimize the ELBO, we estimate the expectation in Equation 8 by drawing samples from $q_\phi(\boldsymbol{u}|\boldsymbol{o}^{(k)})$ and using the reparameterization trick (Kingma et al., 2015) to obtain gradients. A major complication that would normally preclude the use of optimization-based recognition models is the need to differentiate through the mean of the posterior. In this case, this involves differentiating through an entire optimization process. Using automatic differentiation within the iLQR solver is in general impractically expensive memory-wise. However, recent advances in differentiable model predictive control enable implicit differentiation through iLQRsolve with a memory cost that does not depend on the number of iterations (Amos et al., 2018; Blondel et al., 2021; Appendix E).

2.3 Complexity and Implementation

We optimize the ELBO using Adam (Kingma and Ba, 2014) with a decaying learning rate $\propto 1/\sqrt{i}$ where i is the iteration number. Averaging over data samples can be easily parallelized; we do this here using the MPI library and a local CPU cluster. In each iteration and for each data sample, obtaining the approximate posterior mean through iLQR is the main computational bottleneck, with a complexity of $\mathcal{O}(T(n^3+n^2 n_o))$. To help mitigate this cost, we find it useful to re-use the previously inferred control inputs to initialize each iLQRsolve.

3 Experiments and Results

3.1 iLQR-VAE enables fast learning of dynamics

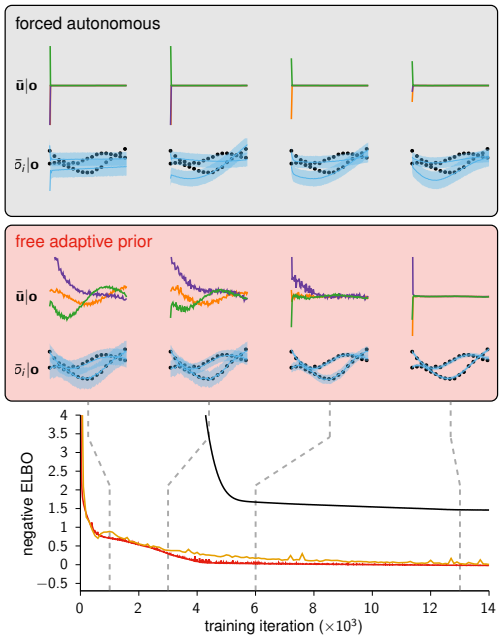

Figure 1: **Fast and robust learning in iLQR-VAE.** Example run of iLQR-VAE on a synthetic dataset generated by an autonomous linear dynamical. iLQR-VAE with an adaptive prior over control inputs (red) uses large inputs to fit the observations initially, but gradually pushes those back into initial conditions as it acquires the ground truth autonomous dynamics. In contrast, iLQR-VAE with a rigid input prior imposing autonomous dynamics throughout learning struggles to learn (black; see text for details). For each setting, insets show the three inferred inputs for a given test trial (top; posterior mean $\bar{\boldsymbol{u}}|\boldsymbol{o}$), and the posterior predictions for the first two corresponding outputs ($\bar{o}_i|\boldsymbol{o}$; black dots: ground truth; blue: posterior mean with 95% c.i.). We also compare learning curves with LFADS (yellow curve). We used the same generator architecture in all scenarios, and the learning rate was hand-tuned for each example.

Before demonstrating the method on a number of synthetic and real datasets involving ongoing external inputs, we begin with a simpler example meant to illustrate some of the main advantages

of iLQR-VAE (Figure 1). We generated data from an autonomous (i.e. non-input-driven) linear dynamical system ($n = 8$, $m = 3$ where n is the number of latents and m the number of input channels) seeded with a random initial condition in each of 56 trials. The state $\boldsymbol{z}_t$ was linearly decoded with added Gaussian noise to produce observation data, which we used to train a model in the same class.

At the beginning of learning, iLQR-VAE originally relies on large ongoing inputs that control the generator into producing outputs very similar to the observations in the data (Figure 1, red box, left), resulting in a rapidly decreasing loss. Subsequently, the amount of input required to fit the observations gradually decreases as the system learns the internal dynamics of the ground truth system. Eventually, the inferred control inputs become confined to the first time bin, i.e. they act as initial conditions for the now autonomous dynamics of the generative model. Thus, iLQR-VAE operates in a regime where the output of the generator explains the data well at all times, and learning consists in make the inputs more parsimonious. We note that this regime is facilitated here by our choice of generator dynamics, which we initialised to be very weak initially and therefore easily controllable.

We contrast this with learning in a modified version of iLQR-VAE where we allowed $\boldsymbol{u}_0$ to vary freely (with a Gaussian prior of adjustable variance) but effectively fixed $\boldsymbol{u}_{t>0}$ to be 0. In other words, we constrained the dynamics of the generator to remain (near-)autonomous throughout learning (Figure 1, grey box, top). Although this incorporates important information about the ground truth generator (which is itself autonomous), counter-intuitively we found that it makes learning worse. Indeed, iLQR is unable to find initial conditions that would explain the data well, resulting in a much higher initial loss. The loss does not decrease as much as in normal iLQR-VAE, indicating that the ground truth dynamics has not been acquired.

On the same toy dataset, we also compare iLQR-VAE to LFADS (Pandarinath et al., 2018), keeping the generative model in the same model class (see Appendix G for details). We find that LFADS learns in a similar manner to iLQR-VAE (Figure 1), also progressively doing away with inputs.

3.2 iLQR-VAE for nonlinear system identification

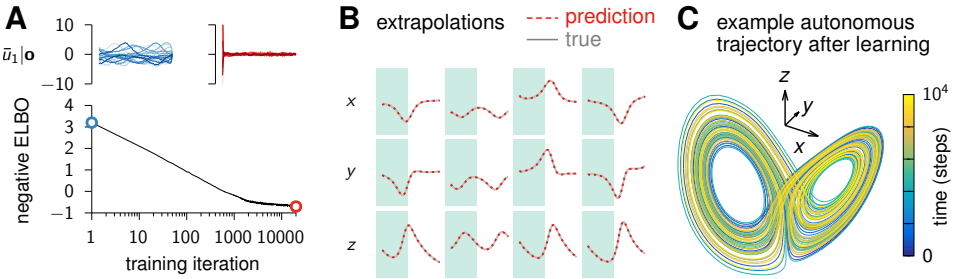

Figure 2: **Learning nonlinear autonomous dynamics.** **(A)** Evolution of the negative ELBO during training of an iLQR-VAE with a nonlinear RNN and a Gaussian likelihood ($n = 20$, $m = 5$, $n_o = 3$). The inputs inferred by iLQR are initially strong (blue, before learning), but are progressively pushed to initial conditions (red, after learning) as the autonomous dynamics of the Lorenz attractor are approximated with increasing accuracy. **(B)** Four example test trajectories (columns), conditioning on the noisy data within the first half (green shading), and predicting in the second half. **(C)** Single long autonomous trajectory after training (setting $\boldsymbol{u}_{t>0} = 0$), starting from a random initial condition and running the dynamics for 10000 steps. The model displays the butterfly topology characteristic of the Lorenz system, and completes multiple cycles without deviating from the attractor, suggesting that the ground-truth dynamics have been learned.

Next, we illustrate the method on an autonomous nonlinear dynamical system, the chaotic Lorenz attractor (Lorenz, 1963; Appendix I). This is a standard benchmark to evaluate system identification methods on nonlinear dynamics (Nguyen et al., 2020; Hernandez et al., 2018; Champion et al., 2019), and one typically considers the dynamics to be learned if the trained model can recreate the whole attractor structure.

Here, we show that iLQR-VAE can learn these complex nonlinear dynamics. Before training, the inferred inputs were large and explained the output observations by forcing the internal state of the generator into appropriate trajectories (Figure 2A, top). At the end of learning, the inputs were confined to initial conditions, with only weak ongoing corrections to the now stronger, near-autonomous dynamics of the generator. In Figure 2B we show that, conditioned on an initial bout of test data, the model perfectly predicts the rest of the trajectory. Moreover, starting from a random initial condition, the model can recreate the whole attractor structure (Figure 2C).

To quantitatively assess how well the dynamics have been learned, we computed the k-step coefficient of determination, R_k^2 (Appendix I), as in Hernandez et al. (2018). This metric evaluates how well the model can predict the true state k steps into the future, starting from any state inferred along a test trajectory. Hernandez et al. reported $R_{30}^2 \approx 1$ but did not show results for larger k. For iLQR-VAE, $R_{30}^2 = 0.998$ and the forward interpolation was still very high at 50 time steps, with $R_{50}^2 = 0.996$.

3.3 Inferring sparse inputs

To demonstrate iLQR-VAE's ability to infer unobserved inputs and learn the ground truth dynamics of an input-driven system, we generated synthetic data from a system with $n = 3, m = 3$ and $n_o = 10$, which evolves with linear dynamics for $T = 1000$ time steps (Figure 3A). The system was driven by sparse inputs, and the output corrupted with Gaussian noise. Input events were drawn in each time step from a Bernoulli distribution with mean $p = 0.03$. Whenever an input event occurred, the magnitude of inputs in each channel was drawn from a standard mutivariate Gaussian distribution.

iLQR-VAE captured most of the variance in these sparse inputs ($R^2 = 0.94 \pm 0.02$; 5 random seeds), and recovered the eigenvalue spectrum of the transition matrix almost perfectly (Figure 3B). We also evaluated LFADS on the same data, using a generator with $n = m = 3$ and linear dynamics, and manually optimized hyperparameters. LFADS performed poorly in this case ($R^2 = 0.05 \pm 0.02$ for input reconstruction; 3 random seeds), as well as in several other similar comparisons on datasets of different sizes and trial numbers (Appendix H). This is unsurprising, as LFADS assumes a dense (auto-regressive Gaussian) prior over the inputs, which is not overridden by the relatively small amount of data used here. Nonetheless, when applied to a set of 56 trials of 100 time steps driven by Gaussian autoregressive inputs, iLQR-VAE still captured the structure in the inputs more accurately than LFADS did ($R^2 = 0.81 \pm 0.01$ vs. 0.29 ± 0.06).

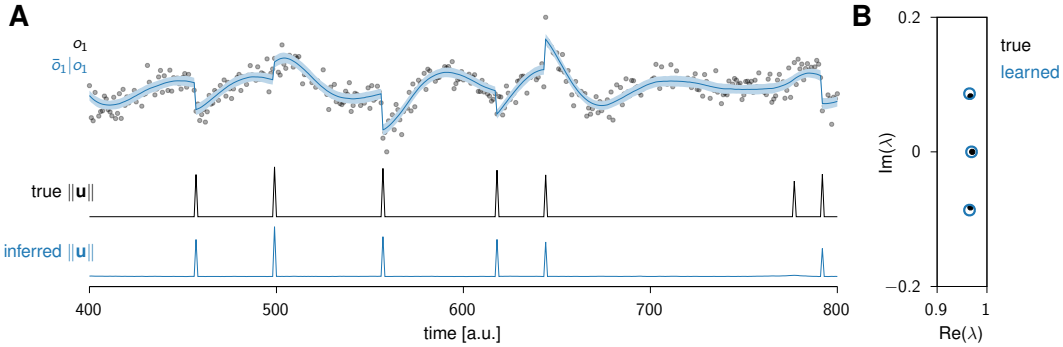

Figure 3: **Inferring sparse inputs to a linear system.** **(A)** Top: example observations (black dots) and inferred posterior mean (blue line). Bottom: true and inferred inputs. iLQR-VAE is able to infer the timing and magnitude of the inputs almost perfectly, despite being trained on only a single timeseries of 1000 time steps. Note that iLQR-VAE fails to infer one of the smallest inputs, whose effect on the observations is largely masked by observation noise. **(B)** Comparison of the true (black) and learned (blue) eigenvalue spectra. This shows that iLQR-VAE recovers the ground-truth dynamical system up to a similarity transformation.

3.4 PREDICTING HAND KINEMATICS FROM PRIMATE M1 RECORDINGS

3.4.1 TRIAL-STRUCTURED MAZE TASK

To highlight the utility of iLQR-VAE for analyzing experimental neuroscience data, we next apply it to recordings of monkey motor (M1) and dorsal premotor (PMd) cortices during a delayed reaching task ('Maze' dataset of Kaufman et al., 2016; DANDI 000128). This dataset contains 108 different reach configurations over nearly 3000 trials, and has recently been proposed as a 'neuroscience MNIST' to benchmark neural data analysis methods (Pei et al., 2021). Several latent variable models were evaluated on this dataset in (Pei et al., 2021), allowing us to directly compare the performance of iLQR-VAE to those reported results.

For this experiment, we fitted iLQR-VAE to the neural activity, using a model with GRU dynamics ($n = 60$), a Student prior over inputs ($m = 15$), and a Poisson likelihood ($n_o = 182$ neurons). To allow for direct comparison with baselines reported in Pei et al. (2021), we trained models on 1340 trials spanning all reach conditions and restricting data to a time window starting 250 ms before and ending 450 ms after movement onset, binned at 5ms.

iLQR-VAE inferred inputs that were confined to initial conditions, from which smooth single-trial dynamics evolved near-autonomously (Figure 4A). As a first measure of performance, we evaluated the model on a "co-smoothing" metric defined as the normalized log-likelihood score of held-out neurons' activity (see Appendix J) conditioned on held-in neurons. Conditioning of 137 neurons (i.e using 45 held-out neurons), we obtained a co-smoothing of 0.331 ± 0.001 (over 5 random seeds). For comparison, Pei et al. (2021) reports 0.187 for GPFA (Yu et al., 2009), 0.225 for SLDS (Linderman et al., 2017), 0.323 for Neural Data Transformers (Ye and Pandarinath, 2021) and $R^2 = 0.331$ for AutoLFADS (LFADS with large scale hyperparameter optimization Keshtkaran et al., 2021) on the same dataset.

Next, we assessed how well hand velocity could be decoded from neural activity (another highly relevant metric for neural data). We applied ridge regression to predict the monkey's hand velocity (with a 100 ms lag) from momentary neuronal firing rates (mean of the posterior predictive distribution) on test data. This reconstruction could be performed with very high accuracy $R^2 = 0.896 \pm 0.002$ (over 5 random seeds), compared to 0.640 for GPFA, 0.795 for SLDS, 0.886 for Neural Data Transformers and 0.910 for AutoLFADS (Pei et al., 2021).

These experiments place iLQR-VAE on par with state-of-the-art methods, without any extensive hyperparameter optimization.

3.4.2 CONTINUOUS REACHING TASK

While a large number of neuroscience studies perform neural and behavioural recordings during trial-structured tasks, much can be learned by analyzing the dynamics of more naturalistic, less constrained behaviours. iLQR-VAE's flexible recognition model is well-suited to the analysis of such less structured tasks, as it can easily be trained and tested on trials of heterogeneous lengths. To illustrate this, we applied iLQR-VAE to a self-paced reaching task during which a monkey had to reach to consecutive targets randomly sampled from a 17x8 grid on a screen (O'Doherty et al., 2018; Makin et al., 2018). This dataset consists of both neural recordings from primary motor cortex (M1) together with continuous behavioural recordings in the form of x- and y-velocities of the fingertip.

In this experiment, we used GRU dynamics ($n = 50$), a Gaussian prior over inputs ($m = 10$), and a combination of a Poisson likelihood (130 neurons) and a Gaussian likelihood (2 kinematic variables). Here, we also experimented with fitting the spike trains and hand velocities jointly, as we found that it allowed iLQR-VAE to reach a similar kinematic decoding performance as when fitting neural activity alone, but using a smaller network. More generally, we reason that a more natural approach to making behavioural predictions from neural data using a probabilistic generator is to fit it to both jointly, and then use the posterior predictive distribution over behavioural variables (conditioning on spike trains only) as a nonlinear decoder. In future work, this could provide more accurate predictions in those motor tasks where linear regression struggles (see e.g. Schroeder et al., 2021).

For our analyses, we used the first ~ 22 minutes of a single recording session (`indy_20160426`), excluded neurons with overall firing rates below 2 Hz, and binned data at 25 ms resolution. Although

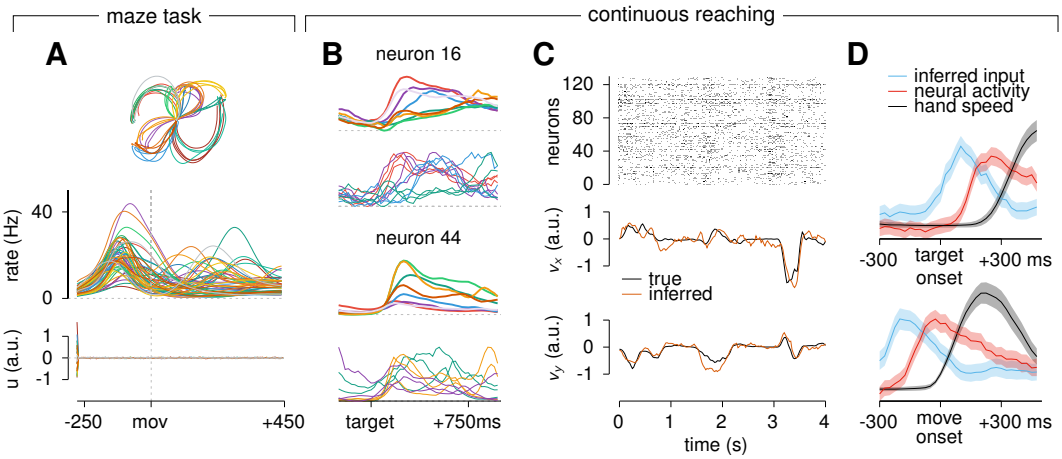

Figure 4: **iLQR-VAE infers smooth firing rates from spiking data, which can be used to accurately decode kinematic variables.** (**A**) 50 example hand trajectories (top) from the monkey reaching 'Maze' dataset, corresponding single-trial firing rate timecourse (middle; one example neuron), and inferred input (bottom; one example input dimension). (**B**) Example spike raster (top) and hand kinematics (bottom) for a 4 second-long chunk of test data in the continuous monkey reaching task. v_x and v_y refer to hand x- and y-velocities respectively. (**C**) Mean (thick) and single-'trial' (thin) firing rates of two example neurons during reaches of various directions (colours), aligned to target onset. Note that three single-'trial' firing rates are shown for only three of the 8 reach directions for which averages are shown. Interestingly, single 'trial' activities evolve tightly around their trial averages, and resembles the firing rate responses shown in A (middle). (**C**) Overall magnitude of the inferred inputs $\|\boldsymbol{u}_t\|$ (blue), average population spiking activity (red), and hand velocity $\|\boldsymbol{y}_t\|$ (black), each z-scored, averaged across movement episodes, and aligned to target onset (top) or movement onset (bottom).

it is not a formal requirement of our method, we chunked the data into 336 non-overlapping pseudo-trials of 4 s each, in order to enable parallelization of the ELBO computation during training. We only trained the model on a random subset of 168 trials.

To highlight the flexibility of iLQR as a recognition model, we then evaluated the model by performing inference on the first 9 minutes of the data, as a single long chunk of observations. Note that this is not generally possible in LFADS or any sequential VAE where an encoder RNN has been trained exclusively on trials of the same fixed length. Despite the lack of trial structure, we found that neurons display a stereotyped firing pattern across multiple instances of each reach. This is revealed by binning the angular space into 8 reach directions, temporally segmenting and grouping the inferred firing rates according to the momentary reach direction, and aligning these segments to the time of target onset (Figure 4B). Moreover, hand kinematics could be linearly decoded from the inferred firing rates with high accuracy (Figure 4C; $R^2 = 0.75 \pm 0.01$ over 5 random seeds), on-par with AutoLFADS ($R^2 = 0.76$; Keshtkaran et al., 2021), and considerably higher than GPFA and related approaches (Jensen et al., 2021).

We next wondered if we could use iLQR-VAE to address an open question in motor neuroscience, namely the extent to which the peri-movement dynamics of the motor cortex rely on external inputs (possibly from other brain areas). Such inputs could arise during movement preparation, execution, neither, or both. We thus examined the relationship between the inputs inferred by iLQR-VAE and the concurrent evolution of the neuronal firing rates and hand kinematics. Overall, neuronal activity tends to rise rapidly starting 150 ms before movement onset (Figure 4D, red), consistent with the literature (Shenoy et al., 2013; Churchland et al., 2012). Interestingly, we found that inputs tend to arise much earlier (around the time of target onset), and start decaying well before the mean neural activity has finished rising (Figure 4D top), about 150 ms before the hand started to move (Figure 4D, bottom). While these results must be interpreted cautiously, as inference was performed using information from the whole duration of the trial (i.e. using iLQR as a smoother), they show that the data is best explained by large inputs prior to movement onset, rather than during movement

itself. Interestingly, the timing of these inputs is globally consistent with target-induced visual inputs driving preparatory activity in M1, whose dynamics then evolve in a more autonomous manner to drive subsequent motion.

4 Discussion

Limitations and future work

While we have demonstrated that iLQR-VAE performs well on various toy and real datasets, the method has a number of limitations that could be addressed in future work. Firstly, using iLQR as a way of solving maximum a posteriori inference in state space models comes at a high computational cost, and with the risk that iLQR may converge to a local minimum. Note that both these issues could potentially be tackled at once if process noise in the generator was modelled separately from control inputs, as the MAP estimation problem could then be solved using some of the highly efficient algorithms available in the framework of linearly solvable stochastic control (Todorov, 2009; Dvijotham and Todorov, 2013; Kappen, 2005). Moreover, for simplicity we modelled posterior input uncertainty using a common covariance across all data samples. This might be limiting, for example when modelling neural populations that exhibit coordinated global firing fluctuations giving rise to data samples with highly variable information content. A better solution would be to amortize the computation of the posterior uncertainty, ideally by reusing some of the computations performed in iLQR. We plan to investigate this in future work.

Conclusion

The rise of new tools and software now makes it possible to record from thousands of neurons while monitoring behaviour in great detail (Jun et al., 2017; Mathis et al., 2018; Musk et al., 2019). These datasets create unique opportunities for understanding the brain dynamics that underlie neural and behavioural observations. However, identifying complex dynamical systems is a hard nonlinear filtering and learning problem that calls for new computational techniques (Kutschireiter et al., 2020). Here, we exploited the duality between control and inference (Toussaint, 2009; Kappen and Ruiz, 2016; Levine, 2018) to bring efficient algorithms for nonlinear control to bear on learning and inference in nonlinear state space models.

The method we proposed uses iLQR, a powerful general purpose nonlinear controller, to perform amortized inference over inputs in an RNN-based generative model. As we highlighted in this work, using an optimization-based recognition model such as iLQR has several advantages. It brings important flexibility at test time, enabling predictions on arbitrary, heterogeneous sequences of observations. Moreover, owing to parameter sharing between the generative and recognition models, learning is made robust (in particular, to initialization) and involves fewer hyperparameters to tune. With the advent of automatically differentiable optimizers (Blondel et al., 2021), we therefore hope that optimization-based recognition models will open up new avenues for VAEs.

References

Amos, B., Rodriguez, I. D. J., Sacks, J., Boots, B., and Kolter, J. Z. (2018). Differentiable MPC for end-to-end planning and control. *arXiv preprint arXiv:1810.13400*.

Archer, E., Park, I. M., Buesing, L., Cunningham, J., and Paninski, L. (2015). Black box variational inference for state space models. *arXiv preprint arXiv:1511.07367*.

Blondel, M., Berthet, Q., Cuturi, M., Frostig, R., Hoyer, S., Llinares-López, F., Pedregosa, F., and Vert, J.-P. (2021). Efficient and modular implicit differentiation. *arXiv preprint arXiv:2105.15183*.

Buesing, L., Macke, J. H., and Sahani, M. (2012). Learning stable, regularised latent models of neural population dynamics. *Network: Computation in Neural Systems*, 23:24–47.

Champion, K., Lusch, B., Kutz, J. N., and Brunton, S. L. (2019). Data-driven discovery of coordinates and governing equations. *Proceedings of the National Academy of Sciences*, 116(45):22445–22451.

Churchland, M. M., Cunningham, J. P., Kaufman, M. T., Foster, J. D., Nuyujukian, P., Ryu, S. I., and Shenoy, K. V. (2012). Neural population dynamics during reaching. *Nature*, 487:51–56.

Churchland, M. M., Cunningham, J. P., Kaufman, M. T., Ryu, S. I., and Shenoy, K. V. (2010). Cortical preparatory activity: representation of movement or first cog in a dynamical machine? *Neuron*, 68(3):387–400.

Cremer, C., Li, X., and Duvenaud, D. (2018). Inference suboptimality in variational autoencoders. In *International Conference on Machine Learning*, pages 1078–1086. PMLR.

Duncker, L., Bohner, G., Boussard, J., and Sahani, M. (2019). Learning interpretable continuous-time models of latent stochastic dynamical systems. In *International Conference on Machine Learning*, pages 1726–1734.

Dvijotham, K. and Todorov, E. (2013). Linearly solvable optimal control. In *Reinforcement learning and approximate dynamic programming for feedback control*, volume 17, pages 119–141. Wiley Online Library.

Gao, Y., Archer, E., Paninski, L., and Cunningham, J. P. (2016). Linear dynamical neural population models through nonlinear embeddings. *arXiv preprint arXiv:1605.08454*.

Ghahramani, Z. and Hinton, G. E. (2000). Variational learning for switching state-space models. *Neural comput.*, 12:831–864.

Hernandez, D., Moretti, A. K., Wei, Z., Saxena, S., Cunningham, J., and Paninski, L. (2018). Nonlinear evolution via spatially-dependent linear dynamics for electrophysiology and calcium data. *arXiv preprint arXiv:1811.02459*.

Jensen, K. T., Kao, T.-C., Stone, J. T., and Hennequin, G. (2021). Scalable bayesian gpfa with automatic relevance determination and discrete noise models. *bioRxiv*.

Jun, J. J., Steinmetz, N. A., Siegle, J. H., Denman, D. J., Bauza, M., Barbarits, B., Lee, A. K., Anastassiou, C. A., Andrei, A., Aydın, Ç., et al. (2017). Fully integrated silicon probes for high-density recording of neural activity. *Nature*, 551(7679):232–236.

Kappen, H. J. (2005). Linear theory for control of nonlinear stochastic systems. *Phys. Rev. Lett.*, 95:200201.

Kappen, H. J. and Ruiz, H. C. (2016). Adaptive importance sampling for control and inference. *Journal of Statistical Physics*, 162:1244–1266.

Kaufman, M. T., Seely, J. S., Sussillo, D., Ryu, S. I., Shenoy, K. V., and Churchland, M. M. (2016). The largest response component in the motor cortex reflects movement timing but not movement type. *Eneuro*, 3(4).

Keshtkaran, M. R., Sedler, A. R., Chowdhury, R. H., Tandon, R., Basrai, D., Nguyen, S. L., Sohn, H., Jazayeri, M., Miller, L. E., and Pandarinath, C. (2021). A large-scale neural network training framework for generalized estimation of single-trial population dynamics. *bioRxiv*.

Kim, T. D., Luo, T. Z., Pillow, J. W., and Brody, C. (2021). Inferring latent dynamics underlying neural population activity via neural differential equations. In Meila, M. and Zhang, T., editors, *Proceedings of the 38th International Conference on Machine Learning*, volume 139 of *Proceedings of Machine Learning Research*, pages 5551–5561. PMLR.

Kingma, D. P. and Ba, J. (2014). Adam: A method for stochastic optimization. *arXiv preprint arXiv:1412.6980*.

Kingma, D. P., Salimans, T., and Welling, M. (2015). Variational dropout and the local reparameterization trick. *arXiv preprint arXiv:1506.02557*.

Kingma, D. P. and Welling, M. (2013). Auto-encoding variational bayes. *arXiv preprint arXiv:1312.6114*.

Kutschireiter, A., Surace, S. C., and Pfister, J.-P. (2020). The hitchhiker's guide to nonlinear filtering. *Journal of Mathematical Psychology*, 94:102307.

Levine, S. (2018). Reinforcement learning and control as probabilistic inference: Tutorial and review. *arXiv preprint arXiv:1805.00909*.

Li, W. and Todorov, E. (2004). Iterative linear quadratic regulator design for nonlinear biological movement systems. In *ICINCO (1)*, pages 222–229. Citeseer.

Linderman, S., Johnson, M., Miller, A., Adams, R., Blei, D., and Paninski, L. (2017). Bayesian learning and inference in recurrent switching linear dynamical systems. In *Artificial Intelligence and Statistics*, pages 914–922. PMLR.

Lorenz, E. N. (1963). Deterministic nonperiodic flow. *Journal of atmospheric sciences*, 20(2):130–141.

Makin, J. G., O'Doherty, J. E., Cardoso, M. M., and Sabes, P. N. (2018). Superior arm-movement decoding from cortex with a new, unsupervised-learning algorithm. *Journal of neural engineering*, 15(2):026010.

Mathis, A., Mamidanna, P., Cury, K. M., Abe, T., Murthy, V. N., Mathis, M. W., and Bethge, M. (2018). Deeplabcut: markerless pose estimation of user-defined body parts with deep learning. *Nature neuroscience*, 21(9):1281–1289.

Musk, E. et al. (2019). An integrated brain-machine interface platform with thousands of channels. *Journal of medical Internet research*, 21:e16194.

Nguyen, D., Ouala, S., Drumetz, L., and Fablet, R. (2020). Variational deep learning for the identification and reconstruction of chaotic and stochastic dynamical systems from noisy and partial observations. *arXiv preprint arXiv:2009.02296*.

O'Doherty, J. E., Cardoso, M. M. B., Makin, J. G., and Sabes, P. N. (2018). Nonhuman Primate Reaching with Multichannel Sensorimotor Cortex Electrophysiology: broadband for indy_20160630_01. This research was supported by the Congressionally Directed Medical Research Program (W81XWH-14-1-0510). JEO was supported by fellowship #2978 from the Paralyzed Veterans of America. JGM was supported by a fellowship from the Swartz Foundation.

Pandarinath, C., O'Shea, D. J., Collins, J., Jozefowicz, R., Stavisky, S. D., Kao, J. C., Trautmann, E. M., Kaufman, M. T., Ryu, S. I., Hochberg, L. R., et al. (2018). Inferring single-trial neural population dynamics using sequential auto-encoders. *Nature methods*, 15(10):805–815.

Pei, F., Ye, J., Zoltowski, D., Wu, A., Chowdhury, R. H., Sohn, H., O'Doherty, J. E., Shenoy, K. V., Kaufman, M. T., Churchland, M., et al. (2021). Neural latents benchmark'21: Evaluating latent variable models of neural population activity. *arXiv preprint arXiv:2109.04463*.

Rezende, D. J., Mohamed, S., and Wierstra, D. (2014). Stochastic backpropagation and approximate inference in deep generative models. In *International conference on machine learning*, pages 1278–1286. PMLR.

Schroeder, K. E., Perkins, S. M., Wang, Q., and Churchland, M. M. (2021). Cortical control of virtual self-motion using task-specific subspaces. *bioRxiv*, pages 2019–12.

She, Q. and Wu, A. (2020). Neural dynamics discovery via gaussian process recurrent neural networks. In *Uncertainty in Artificial Intelligence*, pages 454–464. PMLR.

Shenoy, K. V., Sahani, M., and Churchland, M. M. (2013). Cortical control of arm movements: a dynamical systems perspective. *Annu. Rev. Neurosci.*, 36:337–359.

Stosiek, C., Garaschuk, O., Holthoff, K., and Konnerth, A. (2003). In vivo two-photon calcium imaging of neuronal networks. *Proceedings of the National Academy of Sciences*, 100(12):7319–7324.

Todorov, E. (2009). Efficient computation of optimal actions. *Proc. Natl. Acad. Sci.*, 106:11478–11483.

Toussaint, M. (2009). Robot trajectory optimization using approximate inference. In *Proceedings of the 26th annual international conference on machine learning*, pages 1049–1056.

Ye, J. and Pandarinath, C. (2021). Representation learning for neural population activity with neural data transformers. *bioRxiv*.

Yu, Byron, M., Cunningham, J. P., Santhanam, G., Ryu, S. I., Shenoy, K. V., and Sahani, M. (2009). Gaussian-process factor analysis for low-dimensional single-trial analysis of neural population activity. In *Advances in neural information processing systems*, pages 1881–1888.

Appendix

A GRAPHICAL SUMMARY OF THE MODEL

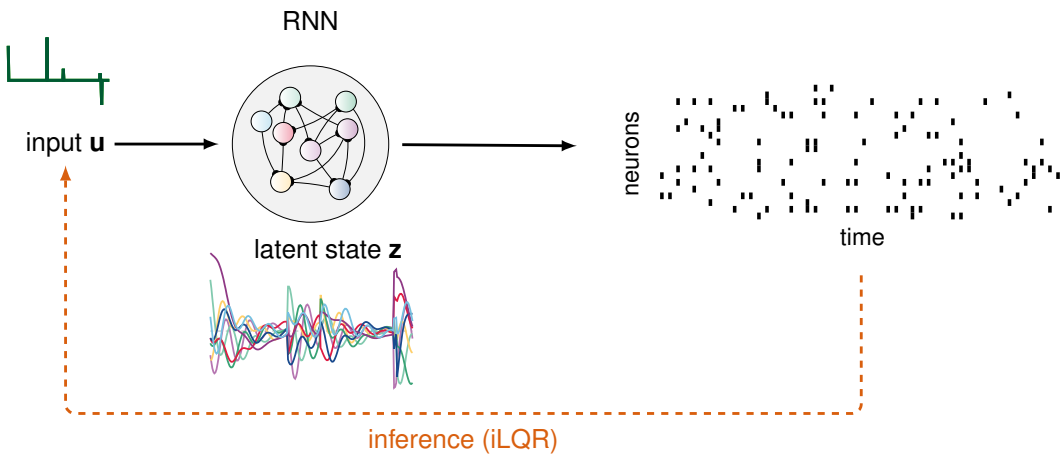

Figure S1: **Illustration of the model** iLQR-VAE is trained to model noisy observations (in this case spiking data), assuming that they are generated by an underlying input-driven dynamical system. Every training iteration involves inference of the input $\boldsymbol{u}$ (green) given observations and the current parameters of the generator. Intuitively, the optimal inputs are ones that produce latent trajectories in the RNN that are most compatible with the data, without overfitting.

B IMPLEMENTATION OF THE DYNAMICS

We considered different functional forms for the discrete-time dynamics of the latent state. In the following, $\boldsymbol{z}_t$ and $\boldsymbol{u}_t$ denote the latent state and an external input at time t, respectively.

B.1 LINEAR DYNAMICS

The simplest case considered is that of linear dynamics:

$$\boldsymbol{z}_{t+1} = \boldsymbol{A}\boldsymbol{z}_t + \boldsymbol{B}\boldsymbol{u}_t \tag{S1}$$

B.2 GRU DYNAMICS

To fit more complex dynamical systems such as the Lorenz or monkey motor cortical data, we used the Minimal Gated Unit (MGU). More specifically, we used the MGU2 variant of the MGU proposed in Heck and Salem (2017):

$$\boldsymbol{f}_t = \sigma(\boldsymbol{U}_f \boldsymbol{z}_{t-1}) \tag{S2}$$
$$\hat{\boldsymbol{z}}_t = g(\boldsymbol{U}_h(\boldsymbol{f}_t \odot \boldsymbol{z}_{t-1}) + \boldsymbol{W}\boldsymbol{x}_t + \boldsymbol{b}_h) \tag{S3}$$
$$\boldsymbol{z}_t = (1 - \boldsymbol{f}_t) \odot \boldsymbol{z}_{t-1} + \boldsymbol{f}_t \odot \hat{\boldsymbol{z}}_{t-1} \tag{S4}$$

where $\odot$ denotes element-wise multiplication, and $\boldsymbol{x}_t = \boldsymbol{B}\boldsymbol{u}_t$ is the input entering the dynamical system. Note that the latent state $\boldsymbol{z}$ is often denoted by $\boldsymbol{h}$ is the literature. We found that the MGU2 gave better and more stable performance than the MGU. We hypothesize that this is due to the input entering the system in the update gate only (as opposed to entering it through both forget and update gates), thus making the system more easily controllable. We chose $g(\cdot)$ to be a soft ReLu-like nonlinearity, $g(x) = (x + \sqrt{x^2 + 4})/2$, and $\sigma(\cdot)$ to be a sigmoid function.

C LIKELIHOOD FUNCTIONS

The likelihood of the observations appear both in the ELBO and in the iLQR cost. Minimization of the latter via iLQR requires computing the momentary Jacobians and Hessians of the likelihood function w.r.t. the internal state $\boldsymbol{z}_t$. Although these quantities can be obtained generically via automatic differentiation, iLQR is always faster when they are provided directly (Appendix D), which we did here using the analytical expressions given below.

C.1 GAUSSIAN LIKELIHOOD

For the Gaussian likelihood, we assumed observations $\boldsymbol{o}$ were linearly decoded from latents $\boldsymbol{z}$, and corrupted with Gaussian noise, such that $\boldsymbol{o} \sim \mathcal{N}(\boldsymbol{C}\boldsymbol{z} + \boldsymbol{b}, \boldsymbol{\Sigma})$, with $\boldsymbol{C}$ the readout matrix, $\boldsymbol{b}$ a vector of biases, and $\boldsymbol{\Sigma}$ a diagonal matrix of variances. This gives the following log-likelihood function:

$$\log P(\boldsymbol{o}_t|\boldsymbol{z}) = -\frac{1}{2}\left[(\boldsymbol{C}\boldsymbol{z}_t + \boldsymbol{b} - \boldsymbol{o}_t)^T \boldsymbol{\Sigma}^{-1}(\boldsymbol{C}\boldsymbol{z}_t + \boldsymbol{b} - \boldsymbol{o}_t) + n_o \log(2\pi) + \sum_i \log \Sigma_{ii}\right] \tag{S5}$$

The Jacobian of this expression is as follows :

$$\frac{\partial \log P(\boldsymbol{o}_t|\boldsymbol{z}_t)}{\partial \boldsymbol{z}_t} = -\boldsymbol{C}^T \boldsymbol{\Sigma}^{-1}(\boldsymbol{C}\boldsymbol{z}_t + \boldsymbol{b} - \boldsymbol{o}) \tag{S6}$$

Finally, the Hessian is given by :

$$\frac{\partial^2 \log P(\boldsymbol{o}_t|\boldsymbol{z}_t)}{\partial \boldsymbol{z}_t \partial \boldsymbol{z}_t^T} = -\boldsymbol{C}^T \boldsymbol{\Sigma}^{-1} \boldsymbol{C} \tag{S7}$$

C.2 POISSON LIKELIHOOD

To model spike trains, we assume that they are generated by a Poisson process with an underlying rate function for neuron i given by:

$$\mu_i = \beta_i f((\boldsymbol{C}\boldsymbol{z})_i + b_i)\,\Delta \tag{S8}$$

where Δ denotes the time bin size and β_i is a neuron-specific gain parameter. This yields the following log-likelihood :

$$\log P(\boldsymbol{o}_t|\boldsymbol{z}_t) = \sum_{i=1}^{n_o}(o_i \log \mu_i - \mu_i + \log o_i!) \tag{S9}$$

where the sum is over neurons. Using the shorthand notations $h(x) = \log f(x)$ and $\boldsymbol{a}_t = \boldsymbol{C}\boldsymbol{z}_t + \boldsymbol{b}$, the Jacobian and Hessian of this expression are given by :

$$\frac{\partial \log P(\boldsymbol{o}_t|\boldsymbol{z}_t)}{\partial \boldsymbol{z}_t} = \boldsymbol{C}^T\left[\boldsymbol{o}_t \odot h'(\boldsymbol{a}_t) - \Delta\,\boldsymbol{\beta} \odot f'(\boldsymbol{a}_t)\right] \tag{S10}$$

$$\frac{\partial^2 \log P(\boldsymbol{o}_t|\boldsymbol{z}_t)}{\partial \boldsymbol{z}_t \partial \boldsymbol{z}_t^T} = \boldsymbol{C}^T\left[\mathrm{diag}(\boldsymbol{o}_t \odot h''(\boldsymbol{a}_t)) - \Delta\,\mathrm{diag}(\boldsymbol{\beta} \odot f''(\boldsymbol{a}_t))\right]\boldsymbol{C} \tag{S11}$$

D iLQR ALGORITHM

Our recognition model makes use of the iterative Linear Quadratic Regulator algorithm (iLQR; Li and Todorov, 2004; Tassa et al., 2014) to find the mean of the posterior distribution $q_\phi(\boldsymbol{u}|\boldsymbol{o})$. Iterative LQR is used to solve finite-horizon optimal control problems with non-linear dynamics and non-quadratic costs by (i) linearizing the dynamics locally around some initial trajectory, (ii) performing a quadratic approximation to the control cost around that same trajectory, (iii) solving the linear-quadratic problem generated by the local approximation to obtain better control inputs, and (iv) repeat until convergence, each time linearizing around the trajectory induced by the new inputs. Below, we first introduce the linear-quadratic regulator (LQR), and detail the approximation used in iLQR to turn any non-linear non-quadratic problem into one that can be solved with LQR. Moreover, we provide pseudo-code for our implementation of iLQR (see Algorithm 1).

The Linear Quadratic Regulator is concerned with finding the set of controls $\boldsymbol{u} \in \mathbb{R}^m$ that minimize a quadratic cost function $\mathcal{C}(\boldsymbol{u})$ under deterministic linear dynamics, given by:

$$\mathcal{C}(\boldsymbol{u}) = \sum_{t=0}^{T} \frac{1}{2}\left(\boldsymbol{z}_t^T \boldsymbol{C}_t^{zz} \boldsymbol{z}_t + \boldsymbol{u}_t^T \boldsymbol{C}_t^{uu} \boldsymbol{u}_t + \boldsymbol{z}_t^T \boldsymbol{C}_t^{zu} \boldsymbol{u}_t + \boldsymbol{u}_t^T \boldsymbol{C}_t^{uz} \boldsymbol{z}_t\right) + \boldsymbol{z}_t^T \boldsymbol{c}_t^z + \boldsymbol{u}_t^T \boldsymbol{c}_t^u \tag{S12}$$

$$\text{s.t. } \boldsymbol{z}_{t+1} = \boldsymbol{A}_t \boldsymbol{z}_t + \boldsymbol{B}_t \boldsymbol{u}_t + \boldsymbol{h}_t. \tag{S13}$$

Here, $\boldsymbol{A}_t \in \mathbb{R}^{n \times n}$ is a (possibly time-dependent) transition matrix, $\boldsymbol{B}_t \in \mathbb{R}^{n \times m}$ represents the input channels at time t, and $\boldsymbol{h}_t$ is a state and input-independent term. Note that while the state $\boldsymbol{z} \in \mathbb{R}^n$ appears in Equation S12, it is a deterministic function of the initial condition $\boldsymbol{z}_0$ and the sequence of inputs $\boldsymbol{u}$. LQR finds the inputs minimizing Equation S12 using a dynamic programming approach, by recursively finding the feedback rule $(\boldsymbol{K}_t, \boldsymbol{k}_t)$ which gives the optimal inputs to minimize the cost-to-go at each time t as $\boldsymbol{u}_t = \boldsymbol{K}_t \boldsymbol{z}_t + \boldsymbol{k}_t$. Details can be found in `function Backward` in Algorithm 1.

iLQR is an extension of LQR to general dynamics and cost functions. Specifically, iLQR minimizes

$$\mathcal{C}_\theta(\boldsymbol{u}) = \sum_{t=0}^{T-1} r_\theta(\boldsymbol{z}_t, \boldsymbol{u}_t, t) \quad \text{subject to} \quad \boldsymbol{z}_{t+1} = \boldsymbol{f}_\theta(\boldsymbol{z}_t, \boldsymbol{u}_t, t) \tag{S14}$$

where θ denotes a set of parameters. At iteration i, iLQR approximates both the dynamics and the cost around the current trajectory $\boldsymbol{\tau}^i = (\boldsymbol{z}^i, \boldsymbol{u}^i)$ as:

$$\tilde{\boldsymbol{f}}_\theta(\delta \boldsymbol{z}_t^i, \delta \boldsymbol{u}_t^i, t) \approx (\nabla_{\boldsymbol{z}} \boldsymbol{f}_\theta)^T \delta \boldsymbol{z}_t + (\nabla_{\boldsymbol{u}} \boldsymbol{f}_\theta)^T \delta \boldsymbol{u}_t \tag{S15}$$

and

$$\tilde{r}_\theta(\delta \boldsymbol{z}_t^i, \delta \boldsymbol{u}_t^i, t) \approx \frac{1}{2}\left[\delta \boldsymbol{z}_t^T (\nabla_{zz}^2 r_\theta) \delta \boldsymbol{z}_t + 2 \delta \boldsymbol{z}_t^T (\nabla_{zu}^2 r_\theta) \delta \boldsymbol{u}_t + \delta \boldsymbol{u}_t^T (\nabla_{uu}^2 r_\theta) \delta \boldsymbol{u}_t\right] \tag{S16}$$

$$+ \delta \boldsymbol{z}^T (\nabla_z r_\theta) + \delta \boldsymbol{u}^T (\nabla_u r_\theta) \tag{S17}$$

Here, $\delta \boldsymbol{z}$ and $\delta \boldsymbol{u}$ refer to perturbations around the current nominal trajectory, and all ∇ operators correspond to partial differentiation evaluated at the current nominal trajectory $(\boldsymbol{u}_t^i, \boldsymbol{z}_i^t)$ and corresponding time t. The above equations are readily identified as a local LQR problem of the form of Equation S12, which can thus be solved using standard dynamic programming tools. Once $\delta \boldsymbol{u}^\star$ minimizing Equation S16 has been computed, the inputs are updated as $\boldsymbol{u}^{i+1} = \boldsymbol{u}^i + \delta \boldsymbol{u}^{\star,i}$, and the new state trajectory follows from simulating the dynamics forward with these new inputs. After each LQR update, we thus obtain a new trajectory $\boldsymbol{\tau}^{i+1}$ and the process repeats until convergence to some locally optimal trajectory $\boldsymbol{\tau}^\star$.

Implementation details can be found in Algorithm 1. Note that the backward LQR pass involves inversion of the matrix $\boldsymbol{Q}_{uu}$ (defined in Algorithm 1 `function Backward`). Depending on the specific form of the iLQR cost function, this might not always be positive-definite. Therefore, we include an adaptive Levenberg-Marquard-type regularizer (not described in the pseudo-code) $\boldsymbol{Q}_{uu} \leftarrow \boldsymbol{Q}_{uu} + \lambda \boldsymbol{I}$ to maintain positive definiteness. Thus, iLQR effectively reverts to first-order gradient descent, as opposed to second-order optimization, whenever the locally quadratic approximation is a bad one.

E DIFFERENTIATING THROUGH iLQR

Here we discuss how to efficiently differentiate through the iLQR algorithm. This becomes necessary when one wishes to differentiate through a function involving an iLQRsolve, such as the posterior mean of our recognition model (Equation 11). While a naive but simple strategy to achieve this would be to unroll the algorithm and gather gradients for every step, this is expensive both computationally and memory-wise. Amos et al. (2018) derived a way to analytically obtain gradients with respect to the parameters of iLQR, at the cost of a single LQR pass. Specifically, differentiating through an iLQRsolve is achieved by running iLQR to convergence, forming a linear-quadratic approximation around the converged trajectory, following the steps described in Appendix D and differentiating through the corresponding LQR problem. Below, we provide an alternative derivation to Amos et al.'s of the gradients of an LQR solution.

Algorithm 1 iLQRsolve($\mathcal{C}_\theta(\boldsymbol{u}), \boldsymbol{u}^{\text{init}}$)), with $\boldsymbol{u} \in \mathbb{R}^m$ and $\mathcal{C}_\theta$ defined in Equation S14.
Parameters: θ, γ

► **iLQR**
$\boldsymbol{\tau}^0$ = Rollout($\boldsymbol{u}^{\text{init}}$)
for $i = 1$ to *converged* **do**
  for $t = 0$ to T **do**
    $\boldsymbol{F}_t^z = \nabla_z \boldsymbol{f}_\theta$, $\boldsymbol{F}_t^u = \nabla_u \boldsymbol{f}_\theta$
    $\boldsymbol{c}_t^z = \nabla_z r_\theta$, $\boldsymbol{c}_t^u = \nabla_u r_\theta$, $\boldsymbol{C}_t^{zz} = \nabla_z^2 r_\theta$, $\boldsymbol{C}_t^{uu} = \nabla_u^2 r_\theta$, $\boldsymbol{C}_t^{uz} = \nabla_{uz}^2 r_\theta$
  end for
  $\boldsymbol{k}_{[0:T-1]}, \boldsymbol{K}_{[0:T-1]}$ = Backward($\boldsymbol{F}_{[0:T]}^z, \boldsymbol{F}_{[0:T]}^u, \boldsymbol{c}_{[0:T]}^z, \boldsymbol{c}_{[0:T]}^u, \boldsymbol{C}_{[0:T]}^{zz}, \boldsymbol{C}_{[0:T]}^{uz}, \boldsymbol{C}_{[0:T]}^{uu}$))
  $\boldsymbol{\tau}^i$ = Forward($\boldsymbol{K}_{[0:T-1]}, \boldsymbol{k}_{[0:T-1]}, \boldsymbol{\tau}^{i-1}$)
end for

◇ **function** Rollout($\boldsymbol{u}$)
$\boldsymbol{z}_0 = \boldsymbol{0}$
for $t = 1$ to T **do**
  $\boldsymbol{z}_{t+1} = \boldsymbol{f}_\theta(\boldsymbol{z}_t, \boldsymbol{u}_t)$
end for
return $\boldsymbol{\tau} = \{\boldsymbol{z}, \boldsymbol{u}\}$

◇ **function** Backward($\boldsymbol{F}_{[0:T]}^x, \boldsymbol{F}_{[0:T]}^u, \boldsymbol{c}_{[0:T]}^z, \boldsymbol{c}_{[0:T]}^u, \boldsymbol{C}_{[0:T]}^{zz}, \boldsymbol{C}_{[0:T]}^{uz}, \boldsymbol{C}_{[0:T]}^{uu}$)
$\boldsymbol{v}_T = \boldsymbol{c}_T^z, \boldsymbol{V}_T = \boldsymbol{C}_T^{zz}$
for $t = T-1$ to 0 **do**
  $\boldsymbol{Q}_t^{zz} = \boldsymbol{C}_t^{zz} + \boldsymbol{F}_t^{z\top} \boldsymbol{V}_{t+1} \boldsymbol{F}_t^z$
  $\boldsymbol{Q}_t^{uz} = \boldsymbol{C}_t^{uz} + \boldsymbol{F}_t^{u\top} \boldsymbol{V}_{t+1} \boldsymbol{F}_t^z$
  $\boldsymbol{Q}_t^{uu} = \boldsymbol{C}_t^{uu} + \boldsymbol{F}_t^{u\top} \boldsymbol{V}_{t+1} \boldsymbol{F}_t^u$
  $\boldsymbol{q}_t^x = \boldsymbol{c}_t^z + \boldsymbol{F}^z \boldsymbol{v}_{t+1}$
  $\boldsymbol{q}_t^u = \boldsymbol{c}_t^u + \boldsymbol{F}^u \boldsymbol{v}_{t+1}$
  $\boldsymbol{K}_t = -\left(\boldsymbol{Q}_t^{uu}\right)^{-1} \boldsymbol{Q}_t^{uz}$
  $\boldsymbol{k}_t = -\left(\boldsymbol{Q}_t^{uu}\right)^{-1} \boldsymbol{q}_t^u$
  $\boldsymbol{V}_t = \boldsymbol{Q}_t^{zz} + \boldsymbol{Q}_t^{zu} \boldsymbol{K}_t$
  $\boldsymbol{v}_t = \boldsymbol{q}_t^z + \boldsymbol{K}_t^T \boldsymbol{q}_t^u$
end for
return $\boldsymbol{k}_{[0:T-1]}, \boldsymbol{K}_{[0:T-1]}$

◇ **function** Forward($\boldsymbol{K}_{[0:T-1]}, \boldsymbol{k}_{[0:T-1]}, \boldsymbol{\tau} = \{\boldsymbol{u}, \boldsymbol{z}\}$)
$\alpha = 1$
repeat
  $\hat{\boldsymbol{z}}_0 = \boldsymbol{0}$
  $\hat{\boldsymbol{u}}_0 = \alpha \boldsymbol{k}_0$
  for $t = 1$ to T **do**
    $\hat{\boldsymbol{z}}_t = f_\theta(\hat{\boldsymbol{z}}_{t-1}, \hat{\boldsymbol{u}}_{t-1})$
    $\hat{\boldsymbol{u}}_t = \boldsymbol{K}_t(\hat{\boldsymbol{z}}_t - \boldsymbol{z}_t) + \alpha \boldsymbol{k}_t$
  end for
  $\alpha = \gamma \alpha$
until $\mathcal{C}_\theta(\hat{\boldsymbol{u}}) < \mathcal{C}_\theta(\boldsymbol{u})$
return $\boldsymbol{\tau} = \{\hat{\boldsymbol{z}}, \hat{\boldsymbol{u}}\}$

E.1 LQR OPTIMALITY CONDITIONS

We now introduce the more compact notation $\boldsymbol{\tau}_t = \begin{bmatrix} \boldsymbol{z}_t \\ \boldsymbol{u}_t \end{bmatrix}$, $\boldsymbol{F}_t = [\boldsymbol{A}_t \quad \boldsymbol{B}_t]$, $\boldsymbol{C}_t = \begin{bmatrix} \boldsymbol{C}_t^{zz} & \boldsymbol{C}_t^{uz} \\ \boldsymbol{C}_t^{zu} & \boldsymbol{C}_t^{uu} \end{bmatrix}$, which will be used in the rest of this section.

As described in Appendix D, the finite-horizon, discrete-time LQR problem involves minimizing:

$$\mathcal{J} = \sum_{t=0}^{T} \left(\frac{1}{2}\boldsymbol{\tau}_t^T \boldsymbol{C}_t \boldsymbol{\tau}_t + \boldsymbol{c}_t^T \boldsymbol{\tau}_t\right) \tag{S18}$$

subject to constraints on its dynamics

$$\boldsymbol{\tau}_{t+1} = \boldsymbol{F}_t \boldsymbol{\tau}_t + \boldsymbol{f}_t, \tag{S19}$$

following the notation from Appendix D. To solve this problem, we write down the Lagrangian:

$$\mathcal{L} = \sum_{t=0}^{T} \left(\frac{1}{2}\boldsymbol{\tau}_t^T \boldsymbol{C}_t \boldsymbol{\tau}_t + \boldsymbol{c}_t^T \boldsymbol{\tau}_t\right) + \sum_{t=0}^{T-1} \boldsymbol{\lambda}_{t+1}^T (\boldsymbol{F}_t \boldsymbol{\tau}_t + \boldsymbol{f}_t - \boldsymbol{x}_{t+1}), \tag{S20}$$

where $\boldsymbol{\lambda}_1, \boldsymbol{\lambda}_2, \cdots, \boldsymbol{\lambda}_T$ are adjoint (dual) variables that enforce the dynamic constraint. Differentiating with respect to $\boldsymbol{\lambda}_t$ and $\boldsymbol{\tau}_t$ enables us to obtain the set of equations satified by $\boldsymbol{\lambda}$ and $\boldsymbol{\tau}$, also known as the KKT conditions (Kuhn and Tucker, 2014; Karush, 2014; Boyd et al., 2004):

$$[\boldsymbol{I} \quad \boldsymbol{0}]\,(\boldsymbol{C}_t \boldsymbol{\tau}_t + \boldsymbol{c}_t) + \boldsymbol{F}_t^T \boldsymbol{\lambda}_{t+1} - \boldsymbol{\lambda}_t = \boldsymbol{0} \tag{S21}$$

$$\boldsymbol{F}_t \boldsymbol{\tau}_t + \boldsymbol{f}_t - [\boldsymbol{I} \quad \boldsymbol{0}]\,\boldsymbol{\tau}_{t+1} = \boldsymbol{0} \tag{S22}$$

$$\boldsymbol{C}_T \boldsymbol{\tau}_T + \boldsymbol{c}_T - [\boldsymbol{I} \quad \boldsymbol{0}]^T \boldsymbol{\lambda}_T = \boldsymbol{0} \tag{S23}$$

$$\boldsymbol{z}_0 - [\boldsymbol{I} \quad \boldsymbol{0}]\,\boldsymbol{\tau}_0 = \boldsymbol{0} \tag{S24}$$

Rearranging, we can rewrite the KKT conditions in matrix form as:

$$\underbrace{\begin{pmatrix} \ddots & & & & & \\ & \boldsymbol{C}_t & \boldsymbol{F}_t^T & & & \\ & \boldsymbol{F}_t & \boldsymbol{0} & [-\boldsymbol{I} \;\; \boldsymbol{0}] & & \\ & & [-\boldsymbol{I} \;\; \boldsymbol{0}]^T & \boldsymbol{C}_{t+1} & \boldsymbol{F}_{t+1}^T & \\ & & & \boldsymbol{F}_{t+1} & \boldsymbol{0} & \\ & & & & & \ddots \end{pmatrix}}_{\boldsymbol{K}} \underbrace{\begin{pmatrix} \vdots \\ \boldsymbol{\tau}_t \\ \boldsymbol{\lambda}_{t+1} \\ \boldsymbol{\tau}_{t+1} \\ \boldsymbol{\lambda}_{t+2} \\ \vdots \end{pmatrix}}_{\boldsymbol{p}} = - \underbrace{\begin{pmatrix} \vdots \\ \boldsymbol{c}_t \\ \boldsymbol{f}_t \\ \boldsymbol{c}_{t+1} \\ \boldsymbol{f}_{t+1} \\ \vdots \end{pmatrix}}_{\boldsymbol{q}} \tag{S25}$$

These optimality conditions are satisfied for the solution to the optimization problem $\boldsymbol{p}^\star = (\boldsymbol{\tau}_0^\star, \cdots, \boldsymbol{\tau}_T^\star, \boldsymbol{\lambda}_1^\star, \cdots \boldsymbol{\lambda}_T^\star)$. Equation S25 implies that the solution of the LQR problem $\boldsymbol{p}^\star$ will satisfy:

$$\boldsymbol{p}^\star = -\boldsymbol{K}^{-1}\boldsymbol{q}. \tag{S26}$$

Computing this quickly becomes infeasible as $\boldsymbol{K}$ grows with long-time horizons, and Equation S25 is typically solved in linear time using a dynamic programming approach, as described in Appendix D.

E.2 BACKPROPAGATING THROUGH THE LQR SOLVER

Differentiating through an LQR solve boils down to differentiating through the backsolve in Equation S26. In the following, we denote the adjoint of parameter $\boldsymbol{\theta}$ as $\bar{\boldsymbol{\theta}}$. From Giles (2008), we know that the adjoint of the backsolve operation is given by:

$$\bar{\boldsymbol{q}} = -\boldsymbol{K}^{-T}\bar{\boldsymbol{p}}, \tag{S27}$$

$$\bar{\boldsymbol{K}} = -\boldsymbol{K}^{-T}\bar{\boldsymbol{p}}\boldsymbol{p}^T = \bar{\boldsymbol{q}}\boldsymbol{p}^T. \tag{S28}$$

We note that Equation S27 has the same form as Equation S26, which means we can compute $\bar{\boldsymbol{q}} = (\cdots, \bar{\boldsymbol{c}}_t, \bar{\boldsymbol{f}}_t, \cdots)^T$ by solving another LQR problem. After solving for $\bar{\boldsymbol{\tau}}$, we can then compute $\bar{\boldsymbol{K}}$ as an outer-product of $\bar{\boldsymbol{z}}$ with $\boldsymbol{y}$ to get:

$$\underbrace{\begin{pmatrix} \ddots & & & & & \\ & \bar{\boldsymbol{K}}_{\boldsymbol{C}_t} & \bar{\boldsymbol{K}}_{\boldsymbol{F}_t^T} & & & \\ & \bar{\boldsymbol{K}}_{\boldsymbol{F}_t} & & & & \\ & & & \bar{\boldsymbol{K}}_{\boldsymbol{C}_{t+1}} & \bar{\boldsymbol{K}}_{\boldsymbol{F}_{t+1}^T} & \\ & & & \bar{\boldsymbol{K}}_{\boldsymbol{F}_{t+1}} & & \\ & & & & & \ddots \end{pmatrix}}_{\bar{\boldsymbol{K}}} \tag{S29}$$

$$= \begin{pmatrix} \vdots \\ \bar{\boldsymbol{c}}_t \\ \bar{\boldsymbol{f}}_t \\ \bar{\boldsymbol{c}}_{t+1} \\ \bar{\boldsymbol{f}}_{t+1} \\ \vdots \end{pmatrix} \begin{pmatrix} \cdots & \boldsymbol{\tau}_t^{\star T} & \boldsymbol{\lambda}_{t+1}^{\star}{}^T & \boldsymbol{\tau}_{t+1}^{\star}{}^T & \boldsymbol{\lambda}_{t+2}^{\star}{}^T & \cdots \end{pmatrix} \tag{S30}$$

$$= \begin{pmatrix} \ddots & & & & & \\ & \bar{\boldsymbol{c}}_t \boldsymbol{\tau}_t^{\star T} & \bar{\boldsymbol{c}}_t \boldsymbol{\lambda}_t^{\star T} & & & \\ & \bar{\boldsymbol{f}}_{t+1} \boldsymbol{\tau}_t^{\star T} & & & & \\ & & & \bar{\boldsymbol{c}}_{t+1} \tau_{t+1}^{\star}{}^T & \bar{\boldsymbol{c}}_{t+1} \boldsymbol{\lambda}_{t+1}^{\star}{}^T & \\ & & & \bar{\boldsymbol{c}}_{t+1} \boldsymbol{\lambda}_{t+1}^{\star}{}^T & & \\ & & & & & \ddots \end{pmatrix}. \tag{S31}$$

Collecting all the gradients of $\bar{\boldsymbol{C}}_t$ and $\bar{\boldsymbol{F}}_t$, we arrive at

$$\bar{\boldsymbol{C}}_t = \frac{1}{2}(\bar{\boldsymbol{K}}_{\boldsymbol{C}_t} + \bar{\boldsymbol{K}}_{\boldsymbol{C}_t}^T) = \frac{1}{2}(\bar{\boldsymbol{c}}_t \boldsymbol{\tau}_t^{\star T} + \boldsymbol{\tau}_t^{\star} \bar{\boldsymbol{c}}_t^T) \tag{S32}$$

$$\bar{\boldsymbol{F}}_t = \bar{\boldsymbol{K}}_{\boldsymbol{F}_t} + \bar{\boldsymbol{K}}_{\boldsymbol{F}_t^T}^T = \bar{\boldsymbol{f}}_{t+1} \boldsymbol{\tau}_t^{\star T} + \boldsymbol{\lambda}_{t+1}^{\star} \bar{\boldsymbol{c}}_t^T. \tag{S33}$$

Note that we have symmetrized the adjoint of $\boldsymbol{C}_t$, which ensures that $\boldsymbol{C}_t$ remains symmetric after each gradient update. The antisymmetric part of $\boldsymbol{C}_t$ does not contribute to the LQR cost.

Finally, one should keep in mind that Equation S19 describes dynamics as a function of τ, as opposed to the locally linearized iLQR dynamics given by Equation S15 which are instead a function of $\delta\tau$. This induces an additional constant in Equation S19, which must be included when computing gradients.

F Link to Kalman filtering

The Linear Quadratic Regulator and the Kalman filter (Kalman, 1964) are algorithms designed for systems with linear dynamics and Gaussian noise. LQR finds the optimal feedback control law to minimize a cost $\mathcal{C}$ in deterministic systems, while the Kalman filter yields an estimate of the state from observations corrupted with process and observation noise. It is well-known that Kalman filtering and LQR are dual of one another, and they can both be combined into LQG to yield an optimal control law from noisy observations. Here, we explore another link between LQR and Kalman smoothing, by showing how LQR can be used as a Kalman smoother. Moreover, in order to gain insights into the learning process of iLQR-VAE, we explore different procedures for learning the parameters of a Kalman filter.

LINEAR QUADRATIC CONTROL AS FILTERING

The Kalman smoother assumes dynamics of the form

$$\boldsymbol{z}_{t+1} = \boldsymbol{A}\boldsymbol{z}_t + \boldsymbol{B}^K \boldsymbol{w}_t \tag{S34}$$
$$\boldsymbol{o}_t = \boldsymbol{C}\boldsymbol{z}_t + \boldsymbol{v}_t \tag{S35}$$

with $\boldsymbol{w} \sim \mathcal{N}(\boldsymbol{0}, \boldsymbol{I})$, $\boldsymbol{v} \sim \mathcal{N}(\boldsymbol{0}, \boldsymbol{\Sigma}_v)$, and the initial condition is assumed to be generated by a Gaussian distribution with known parameters $\boldsymbol{z}_1 \sim \mathcal{N}(\boldsymbol{\mu}, \boldsymbol{\Pi})$.

On the other hand, LQR assumes the following fully-deterministic dynamics :

$$\boldsymbol{z}_{t+1} = \boldsymbol{A}\boldsymbol{z}_t + \boldsymbol{B}^I \boldsymbol{u}_t \tag{S36}$$
$$\boldsymbol{o}_t = \boldsymbol{C}\boldsymbol{z}_t \tag{S37}$$

with $\boldsymbol{z}_1$ known exactly.

Note than in the iLQR-VAE framework we have thus far only considered cases where no observed external inputs were given. However these can be straightforwardly included as an additional $\hat{\boldsymbol{B}}\hat{\boldsymbol{u}}$ term in Equation S36 and Equation S34.

The Kalman smoother's objective is to minimize the expected mean squared error between the inferred latent state and the true state, $\mathbb{E}\left[\|\boldsymbol{x} - \hat{\boldsymbol{x}}\|^2\right]$. As described in Aravkin et al. (2017), with linear dynamics and Gaussian noise, this becomes equivalent to minimizing the following objective w.r.t $\boldsymbol{z}$:

$$\mathcal{L}(\boldsymbol{z}) = \|\boldsymbol{\Pi}^{-1/2}(\boldsymbol{z}_1 - \boldsymbol{\mu})\|^2 + \sum_{t=1}^{T-1} \|\boldsymbol{B}(\boldsymbol{z}_{t+1} - \boldsymbol{A}\boldsymbol{z}_t)\|^2 + \sum_{t=1}^{T} \|\boldsymbol{\Sigma}_{\boldsymbol{v}}^{-1/2}(\boldsymbol{o}_t - \boldsymbol{C}\boldsymbol{z}_t)\|^2 \tag{S38}$$

where the first two terms correspond to the prior over the initial condition and smoothness of the trajectory, and the last term represents the likelihood of the observations. Interestingly, this can be related to the objective we minimize to find the posterior mean in iLQR-VAE (Equation 11):

$$\mathcal{L}(\boldsymbol{u}) = \|\boldsymbol{\Sigma}_0^{-1/2}\boldsymbol{u}_0\|^2 + \sum_{t=1}^{T-1} \|\boldsymbol{\Sigma}_u^{-1/2}\boldsymbol{u}_t\|^2 + \sum_{t=1}^{T} \|\boldsymbol{\Sigma}_{\boldsymbol{v}}^{-1/2}(\boldsymbol{o}_t - \boldsymbol{C}\boldsymbol{z}_t)\|^2 \tag{S39}$$
$$= \|\boldsymbol{\Sigma}_0^{-1/2}\boldsymbol{u}_0\|^2 + \sum_{t=1}^{T-1} \|\boldsymbol{\Sigma}_u^{-1/2}(\boldsymbol{z}_{t+1} - \boldsymbol{A}\boldsymbol{z}_t)\|^2 + \sum_{t=1}^{T} \|\boldsymbol{\Sigma}_{\boldsymbol{v}}^{-1/2}(\boldsymbol{o}_t - \boldsymbol{C}\boldsymbol{z}_t)\|^2. \tag{S40}$$

The right-hand sides of Equation S38 and Equation S39 become identical when $\boldsymbol{\Sigma}_u = \boldsymbol{B}^K$ and $\boldsymbol{\Sigma}_0 = \boldsymbol{\Pi}$. Note that in practice the introduction of the $\boldsymbol{B}^I$ matrix in Equation S34 unties the two formulations slightly by allowing for further mixing between the input channels that isn't accounted for by the prior. In the examples we consider next, we therefore set $\boldsymbol{B}^I = \mathbb{I}$.

The above equations show how LQR can be used to solve the standard Kalman filtering problem, with the key difference being that the optimization is performed over inputs $\boldsymbol{u} = \{\boldsymbol{u}_0, \ldots, \boldsymbol{u}_{T-1}\}$ rather than latent trajectories $\boldsymbol{u} = \{\boldsymbol{z}_1, \ldots, \boldsymbol{z}_T\}$ directly. This is illustrated in Figure S2(A), where a Rauch-Kung-Striebel smoother and LQR were run on the same set of 8-dimensional observations arising from an 8-dimensional linear dynamical system, and inferred the same latent trajectory given the ground-truth parameters. As we only use LQR to parametrize the mean of the posterior distribution, we trained the recognition model for 100 steps to get the uncertainty over the latents, which was very similar to the output of the RKS smoother.

LEARNING A KALMAN FILTER

We proceeded to learn the parameters of the models using either iLQR-VAE, an Expectation-Maximization (EM) procedure, or direct minimization of the negative log likelihood of the data (Figure S2B-C).

Interestingly, the EM algorithm is closely related to iLQR-VAE, since the E-step finds the latent trajectories minimizing Equation S38, when iLQR-VAE solves Equation S39 in an inner optimization loop. While there exists an analytical solution for the M-step in the case of the Kalman filter, this

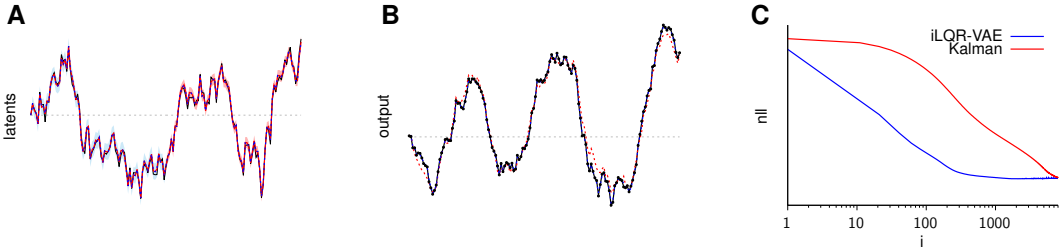

Figure S2: **Comparison of the posterior mean of a Kalman smoother and LQR.** We ran both LQR and a Kalman smoother on noisy observations generated by a latent system (see text for details). **(A)** The Kalman smoother (blue) and LQR (dotted red) both inferred the same posterior mean for the latent trajectories, matching the true latents (black) almost perfectly. The posterior uncertainty is shown for both cases on half of the data. The iLQR-VAE uncertainty was obtained by optimizing the variance of the recognition model for 200 iterations, and then drawing 1000 samples from the recognition model. **(B)** We compared learning the parameters of the posterior distribution using iLQR v.s direct minimization of the NLL. On unseen data, both were able to converge to a solution close to the smoothed output trajectory. Note that we stopped the optimization after 8000 iterations. **(C)** Learning curves of the direct optimization and iLQR-VAE on the same 168 training trials. Note that we used Adam with the same learning rate of 0.02 in both cases, in order to directly compare the effect of the gradient steps. Both x and y axes use a logarithmic scale.

does not generalize to nonlinear dynamics and non-Gaussian noise. Therefore, we used a gradient descent procedure in the M-step.

Both of these were performed using Adam with a learning rate of 0.02, and with initial parameters drawn from the same distributions. We see in Figure S2C that iLQR-VAE reaches a smaller NLL in considerably fewer iterations than gradient descent, which we hypothesize is due to the good preconditioning given by iLQR (discussed in Figure 1). Note however that the cost of one iLQR-VAE iteration is higher than the direct computation of Equation S38.

In this section, we have shown in a simple linear-quadratic example how iLQR-VAE performs filtering by inferring the process noise as inputs. While this is undoubtedly an unconventional approach, it becomes particularly valuable in cases where dynamics are non-linear and the noise non-Gaussian. Indeed, in such cases the problem of learning an estimator for the latent state is a very difficult one, typically solved using methods such as particle filtering or unscented Kalman filters (Doucet and Johansen, 2009; Wan et al., 2001). iLQR-VAE therefore offers another way to solve this problem, with close links to the aforementioned approaches.

G Details of experiment 1

The data in Section 3.1 was generated from an autonomous linear dynamical system with $n = 8$, $m = 3$, and $n_o = 8$ where n_o is the dimension of the observation space. All the models were fit using the dynamics within the ground-truth model class, i.e with linear dynamics, $n = 8$, $m = 3$, and $n_o = 8$. We optimized the model parameters with Adam, using (manually optimized) learning rates of 0.04/(1+ $\sqrt{k/10}$) for the free iLQR-VAE model, 0.04/(1+ $\sqrt{k/10}$ for autonomous iLQR-VAE and 0.02/(1+ $\sqrt{k/30}$ for LFADS, with k the iteration number. We used GRU networks with 32 units to parametrize the LFADS encoders (one encoder for the initial condition and one for the inputs).

H Comparison of LFADS and iLQR-VAE on a toy input inference task

We compared iLQR-VAE and LFADS on several toy datasets of linear dynamical systems of size $n = 3$, driven either by sparse (S) or auto-regressive (AR) 3D inputs, linearly read out onto 10-dimensional observations. We used the LFADS implementation from https://github.com/google-research/computation-thru-dynamics/

tree/master/lfads_tutorial, which we modified to include linear dynamics and Gaussian likelihoods. We then evaluated the quality of the input reconstruction by measuring how much input variance was captured by the models. We report this as the R^2 from inferred to true inputs.

We used a generative model within the ground truth model class. For each dataset, we performed a hyper-parameter search to choose the best-performing encoder architecture and learning rate for LFADS.

Results of this experiment are summarized in Table S1. iLQR-VAE - which did not require any hyperparameter tuning for these examples - inferred inputs more accurately for all dataset sizes and trial lengths.

	LFADS	iLQR-VAE
S 1x1000	0.05 ± 0.03	0.94 ± 0.01
S 10x100	0.15 ± 0.1	0.84 ± 0.01
S 32x100	0.29 ± 0.1	0.83 ± 0.05
S 56x100	0.31 ± 0.08	0.80 ± 0.02
S 10x200	0.27 ± 0.4	0.93 ± 0.01
AR 56x100	0.28 ± 0.02	0.81 ± 0.02

Table S1: Comparison of iLQR-VAE and LFADS on 6 input inference tasks. Results are reported as R^2 (mean $\pm$ sem) over 3 random seeds for each.

Our results suggest that LFADS' performance improves with larger amounts of data. More surprisingly, LFADS also seems to perform better when the data is split into shorter trials. In particular, we found it difficult to fit LFADS on the single long trial, but the dynamics could be learned more accurately this data was split into 10 trials of 100 steps. On the other hand, iLQR-VAE inferred inputs more accurately for longer trials. This is what we would expect if the model is well learnt, as longer trials contain more available information to fit the inputs accurately.

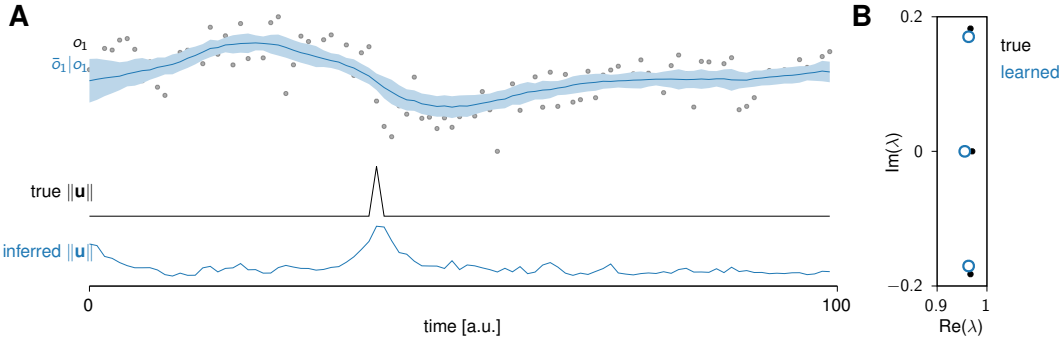

Figure S3: **Details of the sparse input inference in LFADS and iLQR-VAE. (A)** Top: example observations (black dots) and inferred posterior mean (blue line). Bottom: true and inferred inputs. LFADS can infer the timing of the largest input, but also uses non-zero inputs during the rest of the trial. **(B)** Comparison of the true (black) and learned (blue) eigenvalue spectra.

One important distinction between the two methods, which partly explains LFADS' lower R^2, is the prior it over inputs (auto-regressive prior for LFADS and Student for iLQR-VAE). In Figure S3 we show an example of LFADS, on one of the test examples of the S 56x100 dataset. In this example, LFADS infers its largest input concurrently to the ground truth input, but also infers small inputs when there are none in the ground truth. This has a significant impact on the R^2 metric. Note however that this is not the only effect at play here, as emphasized by the lower performance on the AR dataset.

I FURTHER DETAILS OF LORENZ ATTRACTOR

The chaotic Lorenz attractor consists of a three-dimensional state (ℓ_1, ℓ_2, ℓ_3) evolving according to

$$\dot{\ell_1} = 10(\ell_2 - \ell_1) \qquad \dot{\ell_2} = \ell_1(28 - \ell_3) - \ell_2 \qquad \dot{\ell_3} = \ell_1\ell_2 - 8\ell_3/3 \tag{S41}$$

For our example, we generated data by integrating Equation S41 over a long time period using a Runge-Kutta solver (RK4) followed by z-scoring and splitting the resulting state trajectory into 112 non-overlapping bouts (Figure 2A). We added Gaussian noise with a standard deviation of 0.1, and trained iLQR-VAE on this dataset (Figure 2B, bottom). We then fitted these data using GRU dynamics with $n = 20$ and $m = 5$.

The normalized k-step mean-squared error was defined as follows :

$$\text{MSE}_k = \sum_{t=0}^{T-k} \boldsymbol{x}_{t+k} - \hat{\boldsymbol{x}}_{t+k} \tag{S42}$$

$$R_k^2 = 1 - \frac{\text{MSE}_k}{\sum_{t=0}^{T-k}(\boldsymbol{x}_{t+k} - \bar{\boldsymbol{x}})} \tag{S43}$$

where $\hat{\boldsymbol{x}}_{t+k}$ is the prediction at time t+k, and $\bar{\boldsymbol{x}}$ the mean position for this trial.

J FURTHER DETAILS OF SINGLE TRIAL ANALYSES

J.1 BENCHMARKING AGAINST EXISTING METHODS

To allow for direct comparison with benchmarks reported Pei et al. (2021), we first used data provided by the Neural Latents Benchmark (NLB) challenge, available at https://gui.dandiarchive.org/#/dandiset/000128. This data included recordings from 250 ms before movement onset to 450 ms after, binned at 5ms. For regression to hand velocity, we introduced a lag of 100ms between neural activity and hand velocity.

We used 1720 training trials and 510 validation trials, which were drawn randomly for each instantiation of the model, to avoid overfitting to test data. Moreover, iLQR-VAE requires very little hyperparameter optimization, lowering the risk of overfitting to the dataset. As the test data used in the NLB challenge is not publicly available, the results we reported were not computed on the exact same data split. However, the model performed highly consistently across random seeds, such that we expect iLQR-VAE's performance to be directly comparable to the results from Pei et al. (2021).

The co-smoothing metric used to assess how well the model fit the data is defined as log-likelihood score :

$$\frac{1}{n_{sp}\log 2}\left(\mathcal{L}(\boldsymbol{\lambda}; \hat{\boldsymbol{y}}_{n,t}) - \mathcal{L}(\hat{\boldsymbol{\lambda}}_n, \hat{\boldsymbol{y}}_{n,t})\right) \tag{S44}$$

where the overall log-likelihood $\mathcal{L}$ is the sum of all the log-likelihoods evaluated at all points and for all neurons, $\boldsymbol{\lambda}$ denotes the vector inferred time-varying firing rates, $\hat{\boldsymbol{\lambda}}_n$ is the mean firing rate for neuron n and n_{sp} is the total number of spikes.

J.2 LOOKING FOR PREPARATORY INPUTS

A decade of research on the preparation and execution of arm reaches in monkeys has shown that in tasks with explicit delays between target and movement onset, cortical activity is driven into a preparatory subspace during this delay (Churchland et al., 2012; Shenoy et al., 2013; Lara et al., 2018). It has recently been suggested that this could be mediated by inputs during preparation (Kao et al., 2021). To evaluate whether iLQR-VAE could potentially be used to discover systems relying on preparatory inputs, we generated a toy example, modelling a reaching task in which the motor cortex is driven mainly by preparatory inputs and evolves autonomously during movement. More concretely, we generated a network of 40 units with non-normal connectivity, and linearly decoded the neural activity (firing rates) onto a set of torques driving a two-link arm (Todorov et al., 2005). We then defined a task consisting of a 300 ms delay period in which the arm could not move, and

a 300 ms movement phase in which it had to perform a reach to a target. We optimized the inputs to the network such that it was driven by inputs *during the delay period only* (see Figure S4B), yet performed a perfect reach to target. We generated data for 96 different reaches, added Gaussian noise to the neural activity traces (see Figure S4A), and we then trained an iLQR-VAE model with generator dynamics within the ground-truth model class on half of those trials and tested it on the other half. Interestingly, iLQR-VAE learned to model the data using a system mainly driven by preparatory inputs (see Figure S4C). Over all test trials, the ratio of preparatory to movement input magnitudes was 5, suggesting that the learnt dynamical system relied strongly on preparatory inputs.

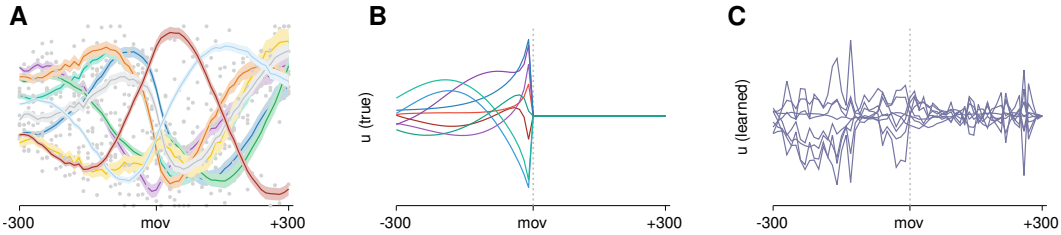

Figure S4: **iLQR-VAE can infer preparatory inputs in a toy linear model.** **(A)** Example firing rates for a given reach (10 neurons shown). **(B)** Example preparatory inputs in the model. **(C)** Example inputs inferred by iLQR-VAE when fitting the data from (A).

The above example suggests that iLQR-VAE is ideally placed to exploit population recordings to investigate hypotheses concerning movement preparation and execution. Thus, we wondered whether preparatory processes could be identified in the neural data; to answer this, we used neural recordings from the Maze dataset, from 500ms before movement onset to 500ms after. We fit these using the same model as described in Section 3.4.1, and found that iLQR-VAE could fit the entire trial by evolving autonomously from the initial condition (Figure S5;B). While unsurprising (Pandarinath et al. (2018) can fit a similar split of data using a fully autonomous GRU), this highlights the difficulty of disentangling parts of the observations that can be explained solely using the model dynamics from those requiring external inputs. We suggest that questions relating to preparatory inputs could nevertheless be answered using methods such as iLQR-VAE, for instance by evaluating the likelihood of the data under different priors.

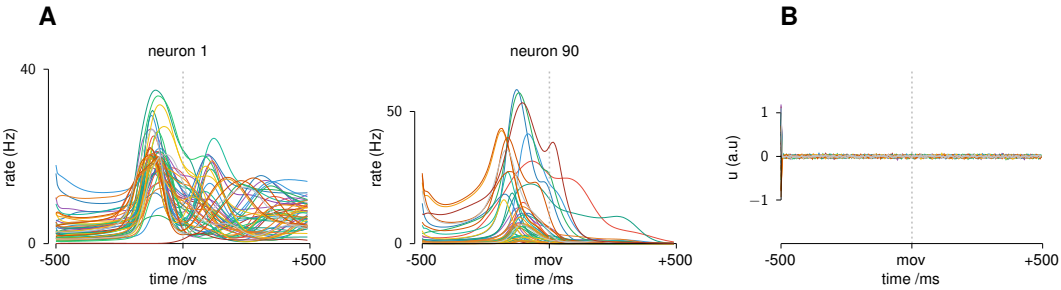

Figure S5: **iLQR-VAE learns to fit both pre-movement and movement activity using a single autonomously evolving dynamical system.** **(A)** Firing rates for neuron 1 (left) and neuron 90 (right) across reaches. Some neurons show more modulation during preparation, while others appear to encode mainly movement-related activity. **(B)** Input inferred by the model.

K Further details of the continuous reaching task analysis

For our analyses of the primate data in Section 3.4, we considered the first 22 minutes of the recording session '`indy_20160426`' from O'Doherty et al. (2018). We binned spikes at 25 ms resolution and considered all neurons with a firing rate of at least 2Hz. The resulting spike counts were square-rooted prior to model fitting. Behavioural data took the form of the velocity of the hand of the monkey in the xy-plane and were extracted as the first derivative of a cubic spline fitted to the position over time. We shifted the hand velocity by 120ms (as this was found to be the optimal lag for decod-

ing in Jensen et al. (2021)), z-scored it, and passed it through a function $f(x) = \text{sign}(x)\log(1+|x|)$ to reduce its sparsity. Note that we undid this transformation to compute the R^2.

To perform our analysis of the inputs to the model after fitting, we defined 'movement onset' after each target onset as the time at which the hand speed first exceeded 0.03 $\text{m}\,\text{s}^{-1}$. Finally we aligned the z-scored input $\boldsymbol{u}$ on each trial to target onset and movement onset separately for visualization purposes. We performed a similar analysis for hand speed and mean z-scored neural activity which were also z-scored and aligned to target and movement onset for comparison with the control input. Note that we inferred inputs over a long chunk (9 minutes) of data, such it was impossible for the model to explain the entire sequence using the initial condition only. Moreover, the absence of trial structure makes it more difficult for the dynamical system to fit the data using the initial condition only, as the dynamics do not unfold in a stereotypical manner during the pseudo-trials.

REFERENCES

Amos, B., Rodriguez, I. D. J., Sacks, J., Boots, B., and Kolter, J. Z. (2018). Differentiable MPC for end-to-end planning and control. *arXiv preprint arXiv:1810.13400*.

Aravkin, A., Burke, J. V., Ljung, L., Lozano, A., and Pillonetto, G. (2017). Generalized kalman smoothing: Modeling and algorithms. *Automatica*, 86:63–86.

Boyd, S., Boyd, S. P., and Vandenberghe, L. (2004). *Convex optimization*. Cambridge university press.

Churchland, M. M., Cunningham, J. P., Kaufman, M. T., Foster, J. D., Nuyujukian, P., Ryu, S. I., and Shenoy, K. V. (2012). Neural population dynamics during reaching. *Nature*, 487:51–56.

Doucet, A. and Johansen, A. M. (2009). A tutorial on particle filtering and smoothing: Fifteen years later. *Handbook of nonlinear filtering*, 12(656-704):3.

Giles, M. (2008). An extended collection of matrix derivative results for forward and reverse mode automatic differentiation.

Heck, J. C. and Salem, F. M. (2017). Simplified minimal gated unit variations for recurrent neural networks. In *2017 IEEE 60th International Midwest Symposium on Circuits and Systems (MWSCAS)*, pages 1593–1596. IEEE.

Jensen, K. T., Kao, T.-C., Stone, J. T., and Hennequin, G. (2021). Scalable bayesian gpfa with automatic relevance determination and discrete noise models. *bioRxiv*.

Kalman, R. E. (1964). When is a linear control system optimal?

Kao, T.-C., Sadabadi, M. S., and Hennequin, G. (2021). Optimal anticipatory control as a theory of motor preparation: a thalamo-cortical circuit model. *Neuron*.

Karush, W. (2014). *Minima of Functions of Several Variables with Inequalities as Side Conditions*. Springer Basel.

Kuhn, H. W. and Tucker, A. W. (2014). Nonlinear programming. In *Traces and emergence of nonlinear programming*, pages 247–258. Springer.

Lara, A. H., Elsayed, G. F., Zimnik, A. J., Cunningham, J. P., and Churchland, M. M. (2018). Conservation of preparatory neural events in monkey motor cortex regardless of how movement is initiated. *eLife*, 7:e31826.

Li, W. and Todorov, E. (2004). Iterative linear quadratic regulator design for nonlinear biological movement systems. In *ICINCO (1)*, pages 222–229. Citeseer.

O'Doherty, J. E., Cardoso, M. M. B., Makin, J. G., and Sabes, P. N. (2018). Nonhuman Primate Reaching with Multichannel Sensorimotor Cortex Electrophysiology: broadband for indy_20160630_01. This research was supported by the Congressionally Directed Medical Research Program (W81XWH-14-1-0510). JEO was supported by fellowship #2978 from the Paralyzed Veterans of America. JGM was supported by a fellowship from the Swartz Foundation.

Pandarinath, C., O'Shea, D. J., Collins, J., Jozefowicz, R., Stavisky, S. D., Kao, J. C., Trautmann, E. M., Kaufman, M. T., Ryu, S. I., Hochberg, L. R., et al. (2018). Inferring single-trial neural population dynamics using sequential auto-encoders. *Nature methods*, 15(10):805–815.

Pei, F., Ye, J., Zoltowski, D., Wu, A., Chowdhury, R. H., Sohn, H., O'Doherty, J. E., Shenoy, K. V., Kaufman, M. T., Churchland, M., et al. (2021). Neural latents benchmark'21: Evaluating latent variable models of neural population activity. *arXiv preprint arXiv:2109.04463*.

Shenoy, K. V., Sahani, M., and Churchland, M. M. (2013). Cortical control of arm movements: a dynamical systems perspective. *Annu. Rev. Neurosci.*, 36:337–359.

Tassa, Y., Mansard, N., and Todorov, E. (2014). Control-limited differential dynamic programming. In *2014 IEEE International Conference on Robotics and Automation (ICRA)*, pages 1168–1175. IEEE.

Todorov, E., Li, W., and Pan, X. (2005). From task parameters to motor synergies: A hierarchical framework for approximately optimal control of redundant manipulators. *Journal of robotic systems*, 22(11):691–710.

Wan, E. A., Van Der Merwe, R., and Haykin, S. (2001). The unscented kalman filter. *Kalman filtering and neural networks*, 5(2007):221–280.